Biophysical Journal
Article

Biophysical Society

Co-Entangled Actin-Microtubule Composites Exhibit Tunable Stiffness and Power-Law Stress Relaxation

Shea N. Ricketts,[1] Jennifer L. Ross,[2] and Rae M. Robertson-Anderson[1,*]
[1]Department of Physics and Biophysics, University of San Diego, San Diego, California and [2]Department of Physics, University of Massachusetts Amherst, Amherst, Massachusetts

ABSTRACT We use optical tweezers microrheology and fluorescence microscopy to characterize the nonlinear mesoscale mechanics and mobility of in vitro co-entangled actin-microtubule composites. We create a suite of randomly oriented, well-mixed networks of actin and microtubules by co-polymerizing varying ratios of actin and tubulin in situ. To perturb each composite far from equilibrium, we use optical tweezers to displace an embedded microsphere a distance greater than the lengths of the filaments at a speed much faster than their intrinsic relaxation rates. We simultaneously measure the force the filaments exert on the bead and the subsequent force relaxation. We find that the presence of a large fraction of microtubules (>0.7) is needed to substantially increase the measured force, which is accompanied by large heterogeneities in force response. Actin minimizes these heterogeneities by reducing the mesh size of the composites and supporting microtubules against buckling. Composites also undergo a sharp transition from strain softening to stiffening when the fraction of microtubules (ϕ_T) exceeds 0.5, which we show arises from faster poroelastic relaxation and suppressed actin bending fluctuations. The force after bead displacement relaxes via power-law decay after an initial period of minimal relaxation. The short-time relaxation profiles ($t < 0.06$ s) arise from poroelastic and bending contributions, whereas the long-time power-law relaxation is indicative of filaments reptating out of deformed entanglement constraints. The scaling exponents for the long-time relaxation exhibit a nonmonotonic dependence on ϕ_T, reaching a maximum for equimolar composites ($\phi_T = 0.5$), suggesting that reptation is fastest in $\phi_T = 0.5$ composites. Corresponding mobility measurements of steady-state actin and microtubules show that both filaments are indeed the most mobile in $\phi_T = 0.5$ composites. This nonmonotonic dependence of mobility on ϕ_T demonstrates the important interplay between mesh size and filament rigidity in polymer networks and highlights the surprising emergent properties that can arise in composites.

INTRODUCTION

The cytoskeleton is a complex network of protein filaments that gives eukaryotic cells structural integrity and shape while enabling cell motility, division, and morphogenesis. Such multifunctional mechanics and processes are possible because of the varying structural properties of cytoskeletal proteins, as well as the interactions between them (1–4). Actin and tubulin are two such proteins that form filaments with very different stiffnesses. Tubulin dimers (~110 kDa) polymerize into 25-nm-wide hollow, rigid microtubules with persistence lengths of $l_p \approx 1$ mm, whereas actin monomers (~42 kDa) polymerize into ~7-nm-wide semi-flexible filaments (F-actin) with $l_p \approx 10$ μm (5–7). At high concentrations, both actin filaments and microtubules form sterically interacting entangled networks with filament dynamics that can be described by the reptation or tube model. Within this framework, each filament is confined to a tube-like region formed by surrounding constraining filaments, and is forced to relax stress by diffusing curvilinearly (i.e. reptating) out of its deformed tube (8,9). The timescale for this process, often termed disengagement, is on the order of minutes to hours for actin and microtubules (10–12). Entangled actin can also partially relax via faster mechanisms such as bending fluctuations (13–15). The entanglement density in networks of actin and microtubules can be characterized by their respective mesh sizes, $\xi_A = 0.3/c_A^{1/2}$ and $\xi_M = 0.89/c_T^{1/2}$, where c_A and c_T are the corresponding protein concentrations in units of mg/mL and the resulting mesh sizes are in units of microns (16–18). As can be seen from these equations, because of the differences in molar mass and filament structure of the two proteins, the mesh size for a

Submitted February 8, 2018, and accepted for publication August 6, 2018.
*Correspondence: randerson@sandiego.edu
Editor: Margaret Gardel.
https://doi.org/10.1016/j.bpj.2018.08.010

microtubule network of a given molarity is ~2× larger than that for actin.

Steric interactions between actin and microtubules within cells directly influence cell shape and mechanics by regulating filament mobility and providing coordinated reinforcement to the cytoskeleton (6,19). Processes such as cell motility and cytokinesis also rely on the physical interactions between these filaments (6,20). Further, although individual microtubules buckle under substantial compressive forces (21–24), steric interactions with the elastic actin network allow microtubules to bear larger compressive loads within the cell (6,11,21,25,26). Studies of composite networks of actin and microtubules are further motivated by materials engineering, in which soft elastic networks are often reinforced with stiff fibers or rigid rods. By tuning the concentration of rigid rods relative to the flexible filaments, bulk properties of composites can be optimized to create lightweight materials with high strength and stiffness (20,27). Such composites also offer enhanced control over large-scale mechanics and increased failure limits tuned by the mechanical differences of the two composite constituents. Finally, composites both in nature and in industry often exhibit emergent properties in which the resulting mechanical properties are not a simple sum of the single-component network mechanics.

In vitro studies of cytoskeleton networks have largely focused on single-component systems of either actin or microtubules (16,18,24,26,28–32). One previous passive microrheology study of an equimolar composite of actin and microtubules showed that although entangled actin solutions appeared incompressible, the composite displayed a finite compressibility resulting from the high stiffness of microtubules (11,33). A previous nonlinear bulk rheology study of cross-linked actin networks doped with low concentrations of microtubules showed that the addition of microtubules led to nonlinear strain stiffening as compared to the signature strain-softening behavior of entangled and weakly cross-linked actin networks (20,34,35). The authors explained this shift as due to stiff microtubules suppressing actin bending modes and local fluctuations, leading to enhanced stretching and affine deformation. Although these few studies revealed important emergent properties in actin-microtubule composites, they were limited in the parameter space of composite makeup. Thus, the question remains as to how the relative concentrations of actin and microtubules impact the mechanical properties of composites. Further, these studies probed the bulk response resulting from large-scale nonlinear strains and the microscopic linear response due to passively diffusing microspheres. Yet, the relevant length scales in actin-microtubule composites are in between these two scales, with persistence lengths of ~10 μm–1 mm, filament lengths of ~5–20 μm, and mesh sizes on the order of a micron. Finally, in these prior studies, composites were created by adding pre-polymerized microtubules to actin rather than polymerizing both proteins together. This method often induces flow alignment of filaments, shearing of microtubules, and bundling of actin filaments, preventing the formation of truly isotropic, well-integrated, co-entangled composites.

Here, we create co-polymerized, co-entangled actin-microtubule composites with systematically varying molar ratios of actin to tubulin. We characterize the nonlinear mesoscale mechanics of composites by pulling optically trapped microspheres a distance of 30 μm through the composites at a rate much faster than the system relaxation rates while measuring the force locally applied to the bead by the composites. These measurements perturb the composites far from equilibrium and are uniquely able to probe possible buckling, rupture, and rearrangement events, as well as micro- and mesoscale spatial heterogeneities. We complement these nonlinear measurements with steady-state image analysis of composites.

METHODS

Rabbit skeletal actin, porcine brain tubulin, and rhodamine-labeled tubulin were purchased from Cytoskeleton (AKL99, T240, TL590M; St. Denver, CO), and Alexa-488-labeled actin was purchased from Thermo Fisher Scientific (A12373; Waltham, MA). To form actin-microtubule composites, varying ratios of unlabeled actin monomers and tubulin dimers were suspended in an aqueous buffer containing 100 mM piperazine-N,N′-bis(ethanesulfonic acid) (pH 6.8), 2 mM $MgCl_2$, 2 mM glycol ether diamine tetraacetic acid, 2 mM ATP, 1 mM GTP, and 5 μM Taxol to a final total protein concentration of 11.3 μM (Fig. 1 *A*). ATP and GTP are required for polymerization of actin and tubulin, respectively. Taxol is used to stabilize microtubules against depolymerization (29). Co-polymerization of both proteins was achieved by incubating the sample for 1 h at 37°C, resulting in well-integrated and stable co-entangled composites (Figs. 1 *B*, S1, and S2). To image composites, 0.13 μM of pre-assembled Alexa-488-labeled actin filaments at a 1:1 labeled:unlabeled monomer ratio and 0.19 μM pre-assembled rhodamine-labeled microtubules at a 1:5 labeling ratio were also added to the solution as tracer filaments (Figs. 1 *B* and S1–S3). Only ~1% of filaments are labeled so as to be able to resolve single filaments within the concentrated three-dimensional (3D) networks. Oxygen scavenging agents (4.5 mg/mL glucose, 0.5% β-mercaptoethanol, 4.3 mg/mL glucose oxidase, 0.7 mg/mL catalase) were added to inhibit photobleaching during imaging (36).

The molar fraction of tubulin in composites, $\phi_T = [tubulin]/([actin] + [tubulin])$ where $[actin]$ and $[tubulin]$ are the molar concentrations of each protein, was varied from 0 to 1. The lengths of actin and microtubules in composites were measured to be 8.7 ± 2.8 and 18.8 ± 9.7 μm, respectively, independent of ϕ_T (Fig. S3). Buffer and incubation conditions were optimized through independent tuning of buffering agents, pH, and nucleotide concentrations as well as incubation time and temperature. Criteria used to assess optimization were 1) both proteins polymerize into filaments ~2–30 μm in length; and 2) networks are isotropic and well-mixed with no visible bundling, aggregation, phase separation, or nematic structure formation. The structure and force response of single-component actin and microtubule networks created using our optimized hybrid conditions are comparable to those formed using standard conditions (Fig. S4). Further details and characterization of optimization methods are described in the Supporting Materials and Methods.

For microrheology measurements (Fig. 1, *C* and *D*), a sparse number of microspheres (beads; Polysciences, Warrington, PA) with diameter $a = 4.5$ μm were added to composites. Before polymerization, the protein and bead mixture was pipetted into a sample chamber made from a glass

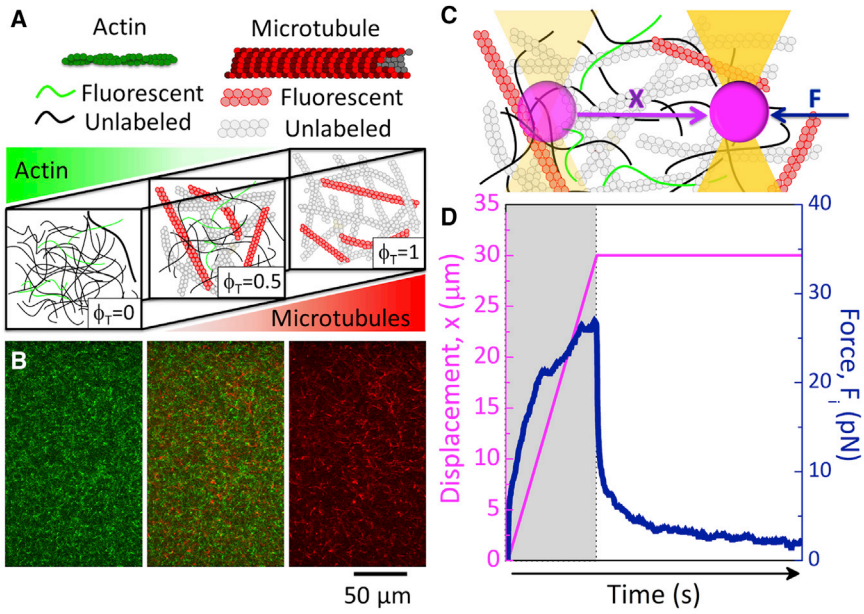

FIGURE 1 Schematic of experimental approach. (*A*) A cartoon of molecular components used in actin-microtubule composites is shown. The tubulin molar fraction, $\phi_T = [tubulin]/([actin] + [tubulin])$, is varied from 0 to 1, with total protein concentration fixed at 11.6 μM. (*B*) To display network architecture, 0.13 μM of actin and 0.19 μM of microtubules are labeled with Alexa-488 (*green*) and rhodamine (*red*), respectively. The images shown are two-color laser scanning confocal micrographs of the actin channel (*green*, *left*), the microtubule channel (*red*, *right*), and an overlay of the two (*middle*) for the $\phi_T = 0.5$ composite. (*C*) For microrheology measurements, an optically trapped microsphere (4.5 μm diameter, not drawn to scale) embedded in the composite is displaced 30 μm (*x*, *magenta*) at a speed of 20 μm/s while the restoring force $F_i(x,t)$ applied to the bead by the composite is measured (*F*, *blue*). (*D*) Sample microrheology data showing the measured Force (*blue*) and bead Displacement (*magenta*) during (*gray region*) and after (*white region*) displacement are depicted. Data shown are for the $\phi_T = 0.5$ composite. To see this figure in color, go online.

slide and coverslip, separated by ~100 μm with double-sided tape to accommodate ~20 μL, and sealed with epoxy. Beads were coated with Alexa-488 BSA (ThermoFisher), following previously described methods (13,37), to inhibit binding interactions with the filaments and visualize beads during measurements. The diameter of the bead was chosen to be large compared to the mesh size of the composites such that the measured force response is reflective of the network rather than the solvent (38–43). In this limit, one can assume that the bead is continuously in contact with a roughly equal number of filaments and does not move through voids in the networks. Specifically, the bead diameter is ~6× larger than the largest mesh size of our composites (0.79 μm, Fig. S5). Thus, at every point during the perturbation, the bead is in contact with ≥12 filaments (~6 filaments each in *y* and *z* directions), assuming the bead encounters a roughly constant *y*-*z* grid of crossing filaments as it moves along *x*, so even at very small bead displacements, our measurements reflect the response of the network rather than individual filaments.

The optical trap used in microrheology measurements was formed using an IX71 fluorescence microscope (Olympus, Shinjuku, Tokyo) outfitted with a 1064 nm Nd:YAG fiber laser (RPMC Lasers, O'Fallon, MO) focused with a 60× 1.4 NA objective (Olympus). A position-sensing detector (First Sensor, Mansfield, MA) measured the deflection of the trapping laser, which is proportional to the force acting on the trapped bead. Trap stiffness was calibrated using the Stokes drag method (44–46). During force measurements, a bead embedded in the composite was trapped and moved a displacement x of 30 μm at a constant speed of $v = 20$ μm/s relative to the sample chamber using a nanopositioning piezoelectric stage (Nano-PDQ; Mad City Labs, Madison, WI) (Fig. 1, *C* and *D*). In comparison to macrorheology experiments, the displacement and speed correspond to a strain of $\gamma = x/a = 6.7$ and strain rate of $\dot{\gamma} = 18^{1/2}(v/a) = 18.9\ s^{-1}$ (38,47). Laser deflection and stage position during and after bead displacement were recorded at a rate of 20 kHz using custom-written Labview code. Post-measurement data analysis was done using custom-written MATLAB software. The response frequency of the stage is 4 kHz, so during the first 0.25 ms, there is some acceleration from 0 to 20 μm/s. Therefore, the initial data points that we evaluate and present in Figs. 1, 2, 3, and 4 occur at $t = 0.25$ ms. For this reason, we measure a nonzero initial force, as the bead has already moved 5 nm (encountering ≥12 filaments). Displayed force curves in Figs. 2 and 4 are averages over an ensemble of 25 different trials, *i*, with each i^{th} trial located in a different region of the network separated by >100 μm. All 25 trials for each composite (shown in Figs. 3 *A* and S6) were carried out in a single sample. However, for each composite, 2–3 different samples were tested to ensure reproducibility of ensemble-averaged quantities. Ensemble-averaged force curves $<F_i(x)>$ are smoothed using a sliding Gaussian blur with a window of 20 data points (1 ms). This smoothing does not result in any detectable change in $<F_i(x)>$ curves but is needed for reducing noise that becomes amplified by computing the numerical derivative of $<F_i(x)>$, $K(x) = d<F_i(x)>/dx$ (Fig. 2, *C* and *D*). Because of the small smoothing window compared to the dynamical timescales of the system, this level of smoothing only serves to reduce electrical and Brownian noise while maintaining the relevant features of each curve (Fig. S7).

To visualize network mobility (Figs. 5, S9, and S10) and architecture (Figs. 1 *B*, S1, and S2), we used a Nikon A1R laser scanning confocal microscope with 60× objective (Nikon, Tokyo, Japan) and QImaging QICAM CCD camera (Surrey, Canada) to collect two-dimensional (2D) images, 2D time series, and 3D images of composites. The microscope has 488 and 532 nm lasers to alternately record separate images in green and red channels to visualize 488-actin and rhodamine-tubulin, respectively. To characterize filament mobility within composites, 512 × 512 pixel time series with a pixel size of 0.41 μm were recorded at 30 fps for 3 min in green and red channels. Post-imaging analysis was carried out using ImageJ/Fiji. Color channels were separated upon import and analyzed separately. To reduce noise, each time series was averaged over every 30 frames, resulting in a 1-fps time series of 180 frames. We computed the standard deviation (σ_I) and mean ($<I>$) of intensity values over all pixels and all frames of each time series. We then computed the coefficient of variation of intensity, $\sigma_I/<I>$, to quantify the mobility of actin and microtubules in each composite while accounting for any systematic intensity differences between movies. We performed this measurement on 3–5 movies from a single sample for each network composition (ϕ_T) and plotted $\sigma_I/<I>$ and the corresponding standard error for the actin and the microtubule channels separately (Fig. 5). To visualize filament mobility, we also created temporal color maps for each movie in which the different colors represent different times during the movie. Color maps in which structures appear mostly white indicate that filaments are largely immobile, whereas the presence of many different colors signifies fluctuations and motion. We compare color maps to 2D images from each movie, which we skeletonize to show the planar network structure (Fig. 5). 2D images also demonstrate that actin and microtubules are well-mixed and co-entangled such that the structural images for both actin and microtubules span the network and are

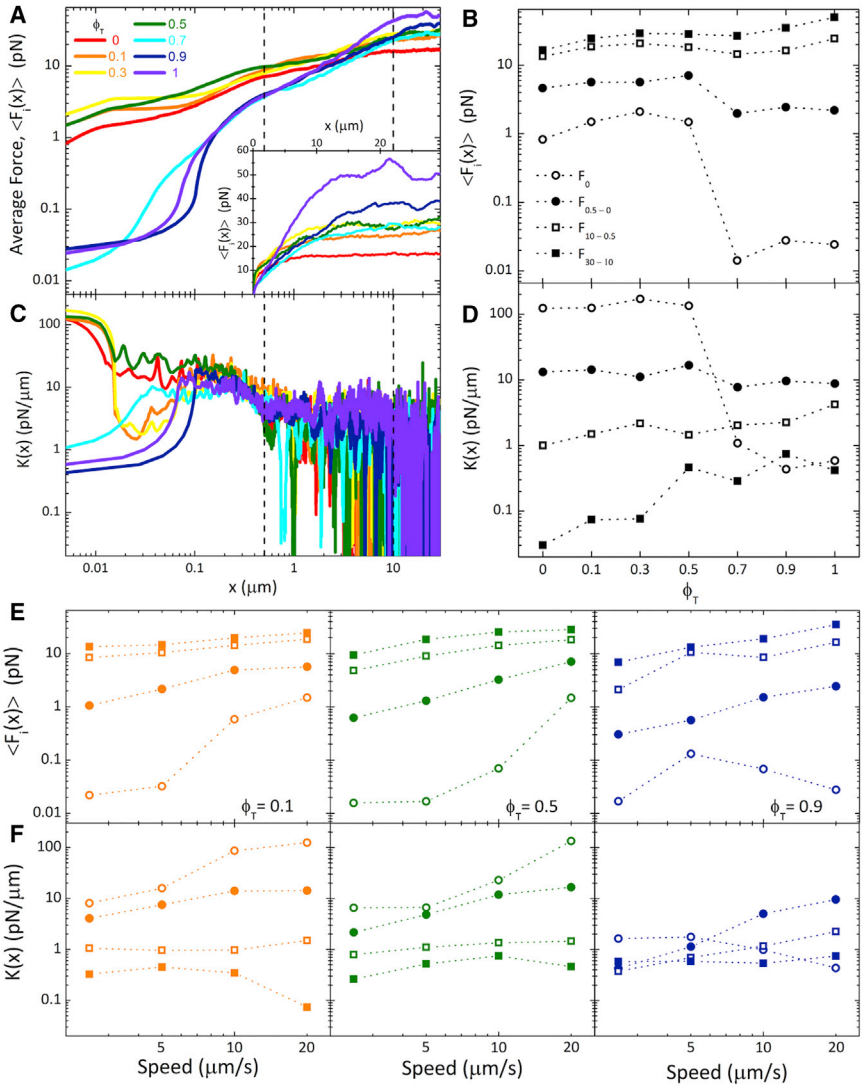

FIGURE 2 Mesoscale force response of actin-microtubule composites display a ϕ_T-dependent crossover from strain-softening to strain-stiffening. (*A*) The ensemble-averaged force $<F_i(x)>$ applied to the moving bead by actin-microtubule composites of varying tubulin molar fraction ϕ_T (listed in legend) is plotted. Data shown are an average over 25 individual (*i*) measurements. Dotted vertical lines denote the displacements over which $<F_i(x)>$ and $K(x)$ are averaged in (*B*) and (*D*). Inset shows $<F_i(x)>$ on a linear scale. (*B*) The initial $<F_i(x)>$ value, F_0 (*open circles*), and the average of $<F_i(x)>$ values plotted over different bead displacements, $x_f - x_i$, denoted as F_{xf-xi}. Displacements of $x_f - x_i = 0.5 - 0$ μm ($F_{0.5-0}$, *closed circles*), 10 – 0.5 ($F_{10-0.5}$, *open squares*), and 30 – 10 (F_{30-10}, *closed squares*) are shown. (*C*) Stiffness, $K(x)$, is calculated as the derivative of the average force with respect to bead displacement ($K(x) = d<F_i(x)>/dx$). (*D*) The initial K value, K_0, and the average of $K(x)$ values plotted over different displacements ($K_{0.5-0}$, $K_{10-0.5}$, K_{30-10}). Displacements and symbol scheme are the same as in (*B*). (*E* and *F*) The dependence of force and stiffness on the speed of the bead displacement for $\phi_T = 0.1$ (*orange*, *left*), 0.5 (*green*, *middle*), and 0.9 (*purple*, *right*) composites is presented. F_0, $F_{0.5-0}$, $F_{10-0.5}$, and F_{30-10} (*E*) and K_0, $K_{0.5-0}$, $K_{10-0.5}$, and K_{30-10} (*F*) are shown as a function of bead speed, with the symbol scheme the same as in (*B*) and (*D*). To see this figure in color, go online.

homogeneously distributed. The sparseness of the 2D structure images are a result of having only ~1% of filaments labeled.

RESULTS AND DISCUSSION

Although actin and microtubules coexist in cells, the standard in vitro polymerization and network formation conditions for the two proteins are incompatible. The few previous studies that have investigated actin-microtubule networks have pre-polymerized and stabilized microtubules with Taxol before adding them to actin monomers to polymerize (3,11), which can lead to flow alignment and rupturing of microtubules upon pipetting into actin monomer solutions and/or the experimental sample chamber. We instead sought to assemble unperturbed co-polymerized networks of actin and microtubules entangled with one another within an experimental sample chamber. To do so, we designed hybrid buffers and polymerization methods detailed in the Methods and Supporting Materials and Methods. Our system includes both ATP and GTP to polymerize actin and tubulin, respectively, as well as the widely used microtubule-stabilization agent Taxol to stabilize microtubules once they polymerize. Although the addition of Taxol likely reduces the stiffness of microtubules compared to those in cells, the reported difference is less than a factor of 10 (29,48), which is well below the ~100-fold difference between the stiffness of microtubules compared to actin. So, we expect our results to also translate to composites without Taxol and to bear physiological relevance. Our methods result in isotropic, well-integrated composite networks of co-entangled actin and microtubules (Figs. 1 *B*, S1, and S2).

We use active microrheology to measure the local nonlinear force response of actin-microtubule composites with varying tubulin molar fractions, ϕ_T. Fig. 2 *A* shows the ensemble-averaged force, $<F_i(x)>$, exerted on optically trapped microspheres as they are pulled a distance x through each composite. We further quantify the length-scale dependence of the force response by averaging $<F_i(x)>$ over

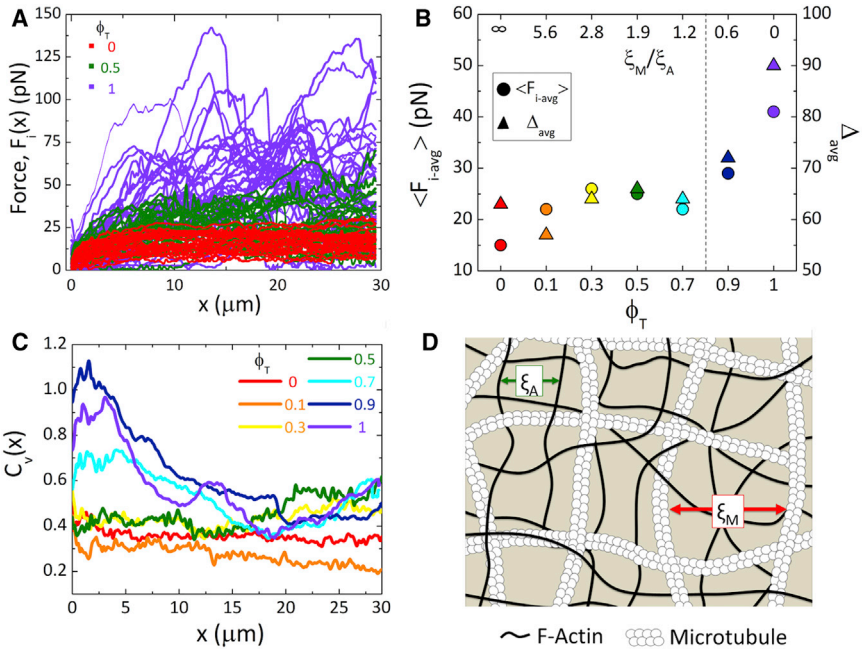

FIGURE 3 Microtubules increase average resistive force and heterogeneity of force response. (*A*) Force curves are shown for all 25 measurements, *i*, of composites with tubulin molar fractions of $\phi_T = 0$ (*red*), 0.5 (*green*), and 1 (*purple*). (*B*) Average force during strain, $<F_{i\text{-}avg}>$, for each composite (*circles*, *left axis*), as well as the corresponding percent range, $\Delta_{avg} = 100*(F_{i\text{-}avg\_max} - F_{i\ \text{-}avg\_min})/(2<F_{i\text{-}avg}>)$ (*triangles*, *right axis*) are shown as a function of ϕ_T (*bottom axis*) and ratio of microtubule mesh size to actin mesh size ξ_M/ξ_A (*top axis*). The dotted vertical line shows when the mesh sizes for both filaments are equal ($\xi_M = \xi_A$). (*C*) The coefficient of variation, $C_V(x) = \sigma_F/<F_i(x)>$, for each ϕ_T as a function of x, shows increasing microscale heterogeneity in the force response with more microtubules. (*D*) An illustration of an equimolar actin-microtubule composite ($\phi_T = 0.5$) is shown. As depicted, the actin mesh size is ~2× smaller than the microtubule mesh, with $\xi_A = 0.6\ \mu$m and $\xi_M = 1.1\ \mu$m. To see this figure in color, go online.

different bead displacements $x_f - x_i$, which we denote as F_{xf-xi}, and comparing to the value measured at $x = 0$, F_0 (Fig. 2 *B*). As shown, composites comprised of mostly actin ($\phi_T \leq 0.5$) exert a ~100× higher initial force, F_0, on the bead than networks comprised of mostly microtubules ($\phi_T > 0.5$). However, the rise in force with x is steeper for $\phi_T > 0.5$ networks such that at ~5 μm, $<F_i(x)>$ becomes larger for $\phi_T > 0.5$ composites compared to $\phi_T \leq 0.5$ (Fig. 2, *A* and *B*). We also evaluate the stiffness of composites, which we quantify by $K(x) = d<F_i(x)>/dx$, in analogy to macrorheology measurements that define the differential modulus K as the derivative of stress with respective to strain (49–51). Increasing and decreasing $K(x)$ values during bead displacement signify strain stiffening and softening, respectively. As shown in Fig. 2 *C*, composites comprised of mostly actin ($\phi_T \leq 0.5$) are initially relatively stiff but quickly soften, whereas $\phi_T > 0.5$ composites display an initially soft/viscous force response followed quickly by strain stiffening. We quantify the length-scale dependence of stiffening/softening by computing x-averaged $K(x)$ values analogous to the force values shown in Fig. 2 *B* (i.e., K_0, $K_{0.5-0}$, $K_{10-0.5}$, K_{30-10}). As shown in Fig. 2 *D*, from 0 to 0.5 μm, the average stiffness increases by an order of magnitude from its initial value for microtubule-rich composites ($\phi_T > 0.5$), whereas it drops by an order of magnitude for $\phi_T \leq 0.5$ composites. For $x > 0.5$ μm, all composites exhibit softening ($K_{0.5-0} > K_{10-0.5} > K_{30-10}$) as the force response approaches a more viscous regime. However, although actin-rich composites exhibit much more initial stiffness (~100× higher K_0), microtubule-rich composites exhibit an order of magnitude higher stiffness at the end of the strain (~10× higher K_{30-10}). We note that the actin-rich composites actually display two types of behavior for a very brief period of the displacement (~0.02–0.06 μm), with the $\phi_T = 0$ and 0.5 composites exhibiting purely softening behavior, whereas the $\phi_T = 0.1$ and 0.3 composites soften more dramatically but then stiffen, such that all $\phi_T \leq 0.5$ composites exhibit similar K values after ~0.06 μm. In future work, we plan to directly focus on the nanoscale response of actin-microtubule composites rather than the mesoscale response to further explore this interesting behavior.

The ϕ_T-dependent stiffening we measure is qualitatively in line with previous bulk rheology results for cross-linked actin networks doped with microtubules. The authors attribute this ϕ_T-dependent stiffening to microtubules suppressing actin bending modes (16,20,52). However, the strain at which stiffening occurs in these studies is ~0.5, which corresponds to a bead displacement of ~2.25 μm in our setup, whereas the stiffening we measure occurs at much smaller strains. At the same time, the strain rate used in these experiments was 0.1 s^{-1} compared to our rate of ~19 s^{-1}. Our comparatively high strain rate could very likely give rise to the stiffening phenomena occurring at much shorter length scales. Further, although stiffening occurs over smaller length scales in our measurements, the stiffness of $\phi_T > 0.5$ composites does not actually become larger than that of $\phi_T \leq 0.5$ composites until ~0.5 μm, with the most pronounced difference occurring for $x > 10$ μm (Fig. 2 *D*). Given that these strains are comparable to those in the macrorheology studies, it is likely suppression of bending modes that gives rise to this increased stiffness at large displacements (K_{30-10}) for microtubule-rich composites. However, our studies show a unique feature not seen

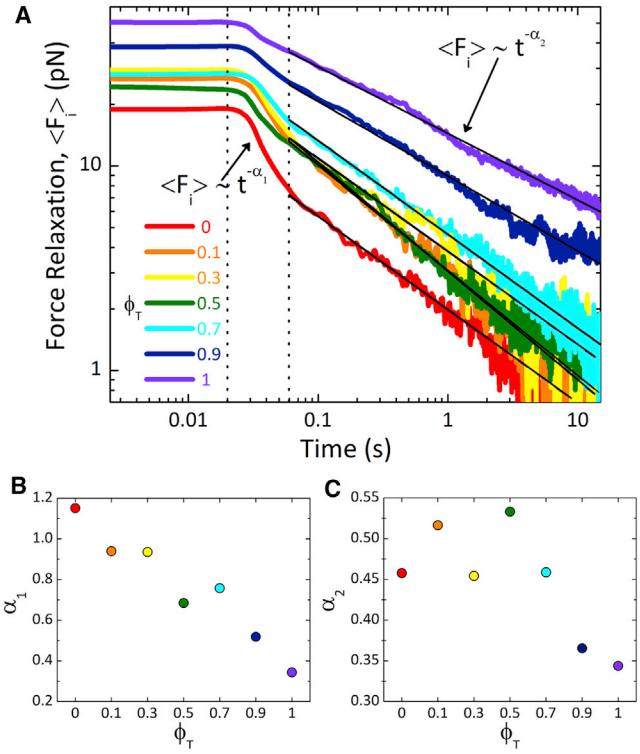

FIGURE 4 Force relaxation of actin-microtubule composites exhibits two-phase power-law decay. (*A*) Relaxation of ensemble-averaged resistive force after bead displacement is shown as a function of time for composites of varying tubulin fractions ϕ_T. The color scheme is the same as in Figs. 2 and 3. Force curves exhibit an initial plateau phase until $t_1 \approx 0.02$ s, after which composites relax via two distinct power-law decays: an initial fast decay ($<F_i> \sim t^{-\alpha_1}$) until $t_2 \approx 0.06$ s, followed by a slow decay ($<F_i> \sim t^{-\alpha_2}$). Vertical dotted lines indicate the crossover timescales t_1 and t_2. Solid black lines are fits of the data to power laws with exponents α_2. (*B*) Estimated scaling exponents α_1 for the fast decay, which decrease proportionally with increasing ϕ_T and become indistinguishable from α_2 when $\phi_T = 1$, are shown. (*C*) Scaling exponents α_2 measured for the second decay phase are shown. Exponents exhibit a nonmonotonic dependence on ϕ_T reaching a maximum value of ~0.53 for $\phi_T = 0.5$. To see this figure in color, go online.

in macrorheology measurements—actin-rich composites are initially much stiffer and exert a much higher force on the bead than those with more microtubules (Fig. 2)—which suggests that we need to consider the differences in the nature of the perturbation in our experiments compared to macrorheology.

In our measurements, the bead is forced to displace water as it moves so it experiences a hydrodynamic drag force as well as the force from the filament network. Especially at very early times, when the filaments have not yet had time to relax or respond to stress, the movement of water through the mesh likely plays an important role in the stress response. In fact, poroelastic models, which consider the dynamics of the mesh as well as the pervading fluid, have been used to accurately describe the stress relaxation of cytoplasm as well as cross-linked polymer hydrogels (53–55). In these models, the faster the timescale for water to drain from the compressed/deformed mesh, the faster the system can relax, such that it will exert a smaller initial force on the bead. The poroelastic timescale is $t_p = ax\eta/2G\xi^2$, where a is the bead diameter, x is the bead displacement, η is the solvent viscosity, and G is the elastic modulus of the network. The elastic modulus of microtubule networks comparable to ours has been measured to be ~1 Pa compared to ~0.1 Pa for comparable actin networks (16,56,57). Further, as described above, the mesh size of microtubule networks is ~2× larger than for actin networks (Fig. S5). Thus, comparison of t_p for actin and microtubule networks gives $t_p(\phi_T = 0)/t_p(\phi_T = 1) = (G_M/G_A)(\xi_M^2/\xi_A^2) \approx 40$. So, water will drain from actin networks ~40× more slowly than from microtubule networks, suggesting that the initial force and stiffness may be comparably higher for actin-rich compared to microtubule-rich composites (Fig. 2). However, this difference will only arise if t_p for actin-rich composites is greater than or comparable to the timescale of the bead displacement, whereas t_p for microtubule-rich composites is shorter than the displacement timescale. For a displacement of $x = 0.01$ μm, we calculate $t_p(\phi_T = 0) \approx 1.2$ ms compared to $t_p(\phi_T = 1) \approx 0.04$ ms. The corresponding timescale for the bead to travel 0.01 μm is 0.5 ms, >12× faster than $t_p(\phi_T = 1)$ and >2× slower than $t_p(\phi_T = 0)$, confirming the important role that poroelasticity plays in the initial force response. The faster draining ability of microtubule networks also enables microtubules to confer compressibility into otherwise nearly incompressible actin networks, as previously reported (27,58).

To further verify this interpretation, we repeated measurements at three slower speeds (2.5, 5, and 10 μm/s) for three of the composites ($\phi_T = 0.1$, 0.5, and 0.9) (Figs. 2, *E* and *F* and S8). Slower bead displacements would allow more time for water to drain from composites, so we should expect to see the initial force and stiffness of actin-rich composites reduced as speed is reduced. On the other hand, we should expect to see minimal difference in F_0 and K_0 values for microtubule-rich networks, as the water has already effectively drained on the timescale of the original perturbation. This effect is exactly what we see for measurements performed at slower speeds (Fig. 2, *E* and *F*). For $\phi_T = 0.1$ and 0.5, composites F_0 and K_0 decrease ~100-fold and >10-fold, respectively, with decreasing speed. For $\phi_T = 0.9$, on the other hand, there is much less change in F_0 and K_0 with no discernible dependence on speed. As we describe below, we find further evidence of poroelasticity in our force relaxation data (Fig. 4).

Previous micro-indentation experiments on cytoplasm have shown that poroelasticity only plays a role in the force response at very short times, after which the filament mesh dominates (55). This effect arises from the fast draining timescale of water compared to the relaxation timescales of the mesh. So, to understand the subsequent ϕ_T-dependent stiffening and softening, we turn to the varying responses of actin compared to microtubules. Actin filaments can bend in

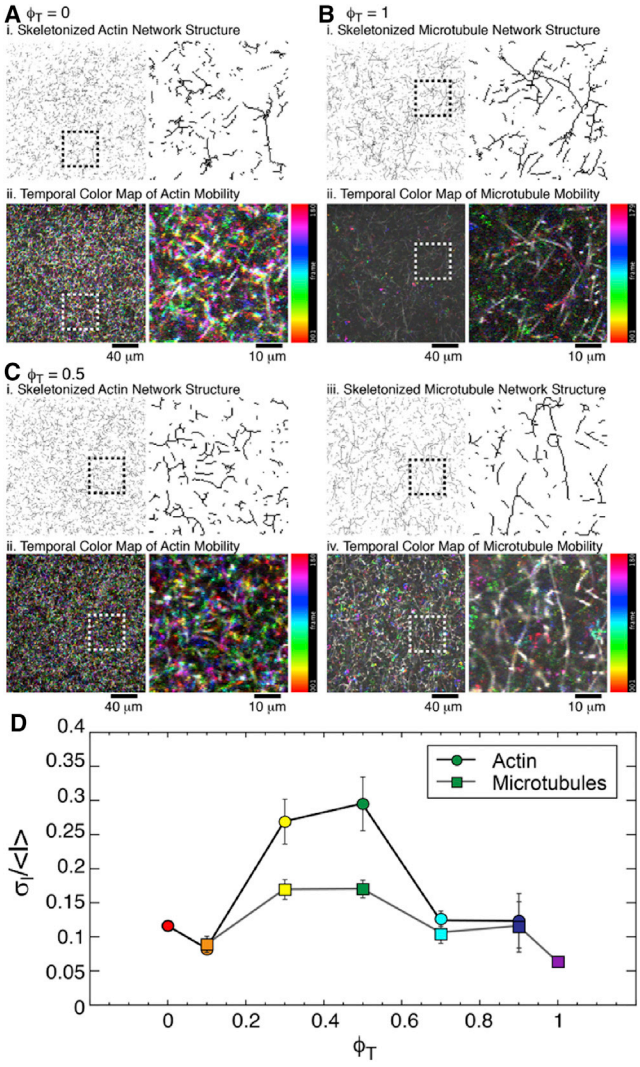

FIGURE 5 Mobility of both actin and microtubules in composites exhibits a nonmonotonic dependence on tubulin fraction. (*A–C*) 2 × 2 images show binary skeletonization of a single frame (*top row*) and temporal color maps (*bottom row*) of movies for (*A*) $\phi_T = 0$, (*B*) $\phi_T = 1$, and (*C*) $\phi_T = 0.5$ networks. Full 512 × 512 images (*left*) as well as zoomed-in images (*right*, corresponding to box in *left-hand* images) are shown. The different colors in temporal color maps correspond to different times during each 180 s movie. Colors go from red at 0 to magenta at 180 s, as shown in the scale bar to the right of each map. (*D*) The standard deviation of intensity values, σ_I, over all pixels and all frames of each time series, normalized by the corresponding mean, $<I>$, versus tubulin fraction ϕ_T, is shown. $\sigma_I/<I>$ is calculated separately for actin and microtubule channels to determine the mobility of each filament in composites. Error bars are the standard error from averaging over 512 × 512 pixels in 3–5 images for each ϕ_T. As shown, the mobility of both actin (*circles*) and microtubules (*squares*) increases as ϕ_T increases to 0.5, followed by a subsequent drop. Color coding represents the different ϕ_T values, as in Figs 2, 3, and 4. To see this figure in color, go online.

response to strain, deforming nonaffinely and sliding off of the moving bead, which can lead to softening after the initial stiff response. Microtubules, on the other hand, cannot readily bend and are instead compressed in the direction of the displacement, building up in front of the bead and increasing the force and stiffness of the response (Fig. 2, *B* and *D*). Further, the amount of stiffening ($K_{0.5-0}/K_0$) for the $\phi_T = 0.9$ composite decreases with decreasing speed, and only exhibits softening for speeds ≤ 5 μm/s. At slower speeds, the microtubules have more time to reorient themselves in response to strain to alleviate stress, further indicating that stiffening is a result of suppressed nonaffine deformations.

As shown in Fig. 3, we also find that increasing the fraction of tubulin in composites increases the heterogeneities in force response. Microscale heterogeneities are displayed by increased noise or "bumpiness" in the individual force curves (Fig. 3 *A*), whereas large-scale heterogeneities can be seen by comparing the force curves for all *i* trials measured in different regions of the sample (separated by >100 μm) (Figs. 3 *A* and S6). Fig. 3 *A*, which shows the individual force curves, $F_i(x)$, for all i measurements for actin networks ($\phi_T = 0$), microtubule networks ($\phi_T = 1$), and $\phi_T = 0.5$ composites, clearly shows that increasing the fraction of microtubules increases heterogeneity at both scales.

This heterogeneity could indicate that the ensemble-averaged quantities presented in Figs. 2 and 4 may misrepresent or mask the system dynamics. However, despite the fact that we see broad distributions of force curves for composites with high ϕ_T, we do not see multiple distinct clusters or distributions of curves (Fig. S6). Rather, all curves appear to be part of a single distribution such that the ensemble average should be a meaningful representation of the data. Nonetheless, to determine how faithfully the ensemble average represents small subsets of the data, we have carried out the analysis shown in Fig. 2 *B* for three randomly chosen trials for $\phi_T = 0$, 0.5, and 1. Although the values calculated from each trial do vary because of the increased noise in the individual curves compared to the ensemble average, the average of the three values is remarkably close to the value determined from the full ensemble-averaged curve (Fig. S6). Thus, the presented ensemble averages appear to be robust quantities that not rely on the full spectrum of curves and meaningfully represent the system dynamics. However, the ϕ_T-dependent breadth of the distributions and noise in individual curves is an important result in and of itself and merits quantitative analysis.

To evaluate the heterogeneity, we first average each $F_i(x)$ over the bead displacement x, which we signify as $F_{i\text{-}avg}$, and calculate the ensemble average, $<F_{i\text{-}avg}>$, as well as the corresponding percent range, $\Delta_{avg} = 100*(F_{i\text{-}avg\_max} - F_{i\text{-}avg\_min})/(2<F_{i\text{-}avg}>)$. As shown in Fig. 3 *B*, we find that the average force ($<F_{i\text{-}avg}>$) is ~3× larger for microtubule networks than that for actin networks, and the corresponding percent range (Δ_{avg}) is doubled. However, surprisingly, the resistive force and heterogeneities do not increase smoothly as ϕ_T increases. Rather, they remain relatively unchanged until the tubulin fraction exceeds 0.7. The large peaks and dips in force curves, partly responsible for the increased Δ_{avg} in microtubule-dominated composites, are suggestive

of microtubule buckling events. Previous studies have shown that microtubules buckle under large compressive loads (23,24), except when they are integrated within the cytoskeletal matrix (21,25,33,59). In line with these results, we interpret the displayed reduced Δ_{avg} and elimination of large dips in the force for $\phi_T < 0.7$ composites as due to the elastic actin network providing reinforcement to microtubules against buckling. Another possibility for the observed dips and peaks is the unbinding of transient filament cross-links, which have been shown to lead to large heterogeneities in force curves (60). We have no cross-linking proteins present in our composites, but divalent cations can cause transient cross-bridges between filaments (61). Although we cannot rule out this possibility, the strong dependence on ϕ_T suggests that the heterogeneities arise solely from microtubules, whereas we would expect cation cross-linking to impact both actin and microtubules (61–63).

To determine if the forces that we impose are sufficient to buckle microtubules at high ϕ_T while preventing them from buckling at low ϕ_T, we calculate the predicted critical force to buckle isolated microtubules, f_{c1}, compared to that for microtubules embedded in an elastic network f_{cN} (25). Isolated microtubules are predicted to buckle at a force $f_{c1} \approx 10\ \kappa/L^2$, where κ is the bending rigidity and L is the length of microtubules, whereas microtubules embedded in a network are predicted to buckle at a force $f_{cN} \approx 4(\kappa G)^{1/2}$, where G is the elastic modulus of the network. Using previously published values for κ (2×10^{-24} Nm (2,48)), our measured L value (~19 μm, Fig. S3), and reported G values for comparable actin networks (~0.1 Pa (57)), we calculate the critical buckling forces to be $f_{c1} \approx 0.05$ pN and $f_{cN} \approx 2$ pN. As described in Methods, we can estimate that the bead is in contact with at least ~12 filaments at each x position along its path, so a minimal force of $F_b \approx 24$ pN would be needed to induce measurable buckling of microtubules in the network. As shown in Fig. 3 *B*, the force at which heterogeneities (Δ_{avg}) begin to increase substantially is ~25 pN, demonstrating that buckling events likely play a principle role in the increased heterogeneity. Further, only above F_b are large dips and peaks observable in force curves. Finally, we find that $<F_{i\text{-}avg}>$ does not increase with increasing ϕ_T for $\phi_T =$ 0.3–0.7. In this range, $<F_{i\text{-}avg}>$ values are all close to F_b, suggesting that intermittent buckling events could be occurring in these composites and releasing some of the network stress. In other words, as ϕ_T increases, the number of buckling events may increase, which in turn would release some resistive force and keep the force from rising appreciably.

The relative mesh sizes of the actin and microtubule networks comprising the composites, as well as the overall "effective" mesh size of the composite, are changing with ϕ_T and could also play a role in the nonlinear dependence of $<F_{i\text{-}avg}>$ on ϕ_T. Larger mesh sizes, or a mesh dominated by rigid rods rather than soft filaments, should result in more heterogeneities, particularly at small length scales. As the number of mesh sizes the bead moves through increases (i.e. as x reaches mesoscopic scales) the differences in the microscale environment should play less of a role in the force response. To quantify the length-scale dependence of our observed heterogeneities, we calculate the standard deviation of $F_i(x)$, $\sigma_F(x)$, as well as the ensemble mean, $<F_i(x)>$, over all i trials for each ϕ_T as function of the bead displacement x. Fig. 3 *C* shows the coefficient of variation, $C_V(x) = \sigma_F/<F_i(x)>$, for each ϕ_T as a function of x. As shown, C_V generally increases with increasing ϕ_T, but only for $\phi_T > 0.5$ is there a substantial increase in C_V. This discrete jump in C_V is most apparent for $x < 10$ μm and becomes negligible for $x > 20$ μm.

The reduced variation in C_V values occurs at nearly the same displacement at which all composites approach a primarily viscous regime ($x \approx 20$ μm) in which F is no longer increasing significantly with x. In this regime, the polymers can flow and deform in response to straining, and stress-induced buckling of microtubules can facilitate rearrangement and flow to release stress. These dynamics likely contribute to reduced heterogeneities. To understand the origin of the microscale heterogeneities causing the increased C_V values at small x, we calculate the predicted mesh size for single-species actin and microtubule networks, ξ_A and ξ_M, at each concentration present in composites. As displayed in the top axis of Fig. 3 *B*, ξ_M/ξ_A remains larger than 1 up to $\phi_T \approx 0.8$, with the actin mesh size ranging from ~6 to 1.25× smaller than that for microtubules. Only at tubulin molar fractions of $\phi_T > 0.7$ do we see a marked increase in $<F_{i\text{-}avg}>$, Δ_{avg}, and C_V as the microtubule mesh size becomes smaller than that for actin ($\xi_M/\xi_A < 1$). Up to $\phi_T \approx 0.8$, a tighter, more entangled actin network pervades the system, which could suppress the heterogeneities caused by larger, more rigid microtubules (Fig. 3 *D*). We can also quantify an "effective" composite mesh size ξ_C by considering the density of mesh-sized volumes in each composite, $\xi_C = (\xi_M{}^{-3} + \xi_A{}^{-3})^{-1/3}$ (Fig. S5). We find that ξ_C increases from 0.42 to 0.79 μm with increasing ϕ_T, with the value remaining close to ξ_A until $\phi_T \approx 0.8$. So, although semiflexible actin filaments are being replaced by rigid microtubules, the decrease in the density of entanglements offsets the increase in filament rigidity such that the resistive force and heterogeneities remain relatively unchanged until $\phi_T > 0.7$.

We also characterize the relaxation of the applied force on the bead after the displacement. As shown in Fig. 4 *A*, the force relaxations for all composites display power-law relaxation in time ($<F_i> \sim t^{-\alpha}$) after an initial time-independent plateau. The initial plateau, in which no force dissipates, persists until $t_1 \approx 0.02$ s, after which all networks with actin present undergo a very brief ϕ_T-dependent decay phase that lasts until $t_2 \approx 0.06$ s. Although the small timescale of this phase prohibits accurate quantification of its functional form (64), if we estimate as power law, we can

extract approximate scaling exponents that we find decrease roughly linearly with increasing fractions of tubulin (Fig. 4 *B*). At $t_2 \approx 0.06$ s, the relaxations for all networks transition to slower power-law decay with exponents of $\alpha_2 \approx 0.34$–0.53 that display a nonmonotonic dependence on ϕ_T, reaching a maximum at $\phi_T = 0.5$ (Fig. 4 *C*).

These unique relaxation characteristics are in opposition to the expected dynamics for entangled polymer systems, in which force relaxation is typically described by a sum of exponential decays due to distinct relaxation mechanisms with well-separated timescales (13,65). Power-law relaxation suggests that there is a wide spectrum of relaxation times that are not well separated (66). Such spectra can arise from a distribution of filament lengths, stiffnesses, and mesh sizes; or from temporal evolution of relaxation mechanisms such that the corresponding timescales are changing in time (67). Our composites indeed have a distribution of macromolecular properties and responses to applied force (Fig. S6), so power-law relaxation is not entirely surprising. Yet, the initial plateau, the ϕ_T-independent crossover times, and the ϕ_T-dependent scaling exponents all warrant further discussion.

The initial plateau, in which there is no force dissipation, suggests that there are no available relaxation mechanisms that the filaments can undergo on these timescales. Previous micro-indentation experiments on cytoplasm found that force relaxation also exhibited an initial plateau followed by power-law relaxation. Authors showed that the short-time plateau behavior could be fit to a poroelastic model but that this model failed for longer times in which the relaxation was distinctly power law as opposed to a stretched exponential (55). The agreement between our early-time relaxation and that of poroelastic cytoplasm is not only further evidence that our short-timescale stress response described above (Fig. 2) can be described in terms of poroelasticity, but also suggests that our composites can indeed be used to shed light on cellular mechanics.

Once the timescale has become longer than that of the fastest relaxation mode of the network, filament relaxation should dominate the response over poroelastic fluid draining. We can estimate the fastest relaxation time of our composites as that of the fastest predicted actin relaxation mode, which is the time for length scales comparable to the mesh size to relax (68,69). This actin mesh time, $\tau_{m,A} \approx \beta\zeta{\xi_A}^4{l_p}^{-1}$, where $\beta = 1/k_BT$ and ζ is the translational friction coefficient (10,70), can be understood as the time it takes for hydrodynamic interactions between filaments to become important. For $\phi_T = 0$ networks, $\tau_{m,A} \approx 0.01$ s, which is quite close to the time at which power-law relaxation begins (t_1). Our measurements carried out at slower speeds all show the same initial plateau and timescale t_1 for relaxation to ensue, demonstrating that t_1 is an intrinsic timescale of the system rather than an artifact of the loading rate.

To understand the fast relaxation that occurs at $t_1 < t < t_2$, we evaluate the next relevant relaxation timescale in the system, which is the actin entanglement time $\tau_{e,A} \approx \beta\zeta{\xi_A}^{3.2}{l_p}^{-0.2}$ (10). This is the time at which each actin filament begins to "feel" its entanglement tube and undergo reptation to relax stress. For $t < \tau_{e,A}$, entangled semiflexible actin can relax stress via bending fluctuations, which are less accessible to more rigid microtubules (13,15). For $\phi_T = 0$ networks, $\tau_{e,A} \approx 0.07$ s, which is markedly close to our measured crossover time $t_2 \approx 0.06$ s. This finding, along with the fact that α_1 scales roughly linearly with the fraction of actin in composites, suggests that the relaxation occurring between ~0.02 and 0.06 s is due to actin bending modes. These nonaffine bending deformations (16) have been shown to result in stress softening rather than stiffening behavior. The clear transition to stiffening behavior as ϕ_T increases is further evidence that this fast relaxation mode is due to actin bending fluctuations that microtubules increasingly suppress as ϕ_T increases. We note that it is possible that ϕ_T-dependent reduction in α_1 is simply a result of fewer actin filaments in the network, so the bending fluctuations contribute less to the overall relaxation, rather than microtubules actively suppressing bending modes. In either case, as ϕ_T increases, the degree to which the composites can relax via bending is reduced. We also note that this fast relaxation mode does not appear to be present in our measurements of similar actin networks in standard actin network buffer conditions (Fig. S4). However, previous measurements on comparable actin networks in standard buffer conditions have reported evidence of fast relaxation modes arising from bending (14,15).

We interpret our final relaxation phase, which begins at $t_2 \approx \tau_{e,A}$, as arising from reptation and tube disengagement. As described above, for $t > \tau_e$, fast relaxation modes become negligible and filaments relax primarily via reptation out of deformed entanglement tubes (i.e. disengagement). Previous studies have shown that entangled biopolymer networks subject to nonlinear strains can exhibit power-law force relaxation arising from tube disengagement (47,71). In previous microrheology experiments on entangled actin, force relaxation transitioned from exponential to power law, with a scaling exponent of ~0.5, when the bead speed exceeded ~3 μm/s (71). Our final phase scaling exponents ($\alpha_2 \approx 0.34$–0.53) are very close to this previously reported value, as well as to predictions based on a non-classical disengagement mechanism for entangled polymers subject to nonlinear strains (67,71,72). Within this framework, nonlinear strains dilate entanglement tubes such that, after strain, tubes shrink back to their original size over the same timescale that filaments reptate out of the deformed tubes. The result is that as each filament attempts to reptate out of its tube, the characteristic disengagement time grows longer, thereby producing power-law decay. Our measurements carried out at slower speeds show that composites transition from power-law to exponential relaxation at speeds of 2.5–5 μm/s (Fig. S8), similar to the previously reported crossover speed (71). This result is further

evidence that the power-law relaxation is due to the nonlinear nature of the perturbation and the corresponding non-classical time-dependent tube confinement.

Although we cannot rule out contributions from the heterogeneous nature of the composites to the power-law behavior, the agreement with previously reported scaling exponents, the ϕ_T-independent crossover time ($t_2 \approx \tau_{e,A}$), and the transition to exponential scaling at slow speeds all indicate that the power law arises from the non-classical time-dependent tube confinement. Further, our analysis on individual force curves (Fig. S6) shows that the power-law scaling is preserved for individual trials and that similar exponents are calculated from a small subset of trials compared to the full ensemble average.

The surprising nonmonotonic dependence of α_2 on ϕ_T, which had not been previously reported or predicted, suggests that reptation proceeds most quickly in equimolar composites ($\phi_T \approx 0.5$) compared to networks of actin or microtubules alone. This result could arise from the competition between the increase in ξ_C and the increase in filament rigidity as ϕ_T increases, as we describe above. Namely, although semiflexible actin filaments, which can reptate more quickly, are being replaced by slower rigid microtubules, the decrease in the density of entanglements offsets the increase in filament rigidity such that the force decay is steepest for intermediate ϕ_T values. This competition also likely contributes to the nonlinear dependence of the average force on ϕ_T during perturbation (Fig. 3 *B*). Specifically, as the fraction of microtubules increases, the measured force remains roughly constant until $\phi_T > 0.7$, despite the increasing rigidity of the system as ϕ_T increases. Although network rigidity increases, which would increase resistive force, the mesh size is also increasing, allowing filaments to more easily move to alleviate stress, offsetting this resistance.

To shed more light on this surprising nonmonotonicity and to correlate the measured nonlinear stress characteristics with the corresponding steady-state dynamics, we quantify the mobility of actin and microtubules in steady-state composites by analyzing time series acquired using two-color fluorescence confocal microscopy (Figs. 5, S9, and S10). As described in Methods, we use the coefficient of variation of pixel intensities over time, $\sigma_I / \langle I \rangle$, as a measure of mobility. We also examine temporal color maps of acquired movies to discern variations in mobility. As shown in Fig. 5, the mobility of both actin and microtubules within composites display a nonmonotonic dependence on tubulin fraction. Namely, mobility increases as ϕ_T increases to 0.5 after which it decreases. This effect can also be seen in the temporal color maps which show more color for $\phi_T = 0.5$ composites compared to $\phi_T = 0$ or $\phi_T = 1$ networks. This nonmonotonicity is quite similar to that of α_2, demonstrating that the magnitudes of α_2 correlate with filament mobility. The drop in mobility for $\phi_T > 0.5$ occurs at the same tubulin fraction at which composites transition from strain softening to stiffening ($\phi_T \approx 0.7$), supporting the evidence that stiffening arises from suppressed filament fluctuations. The increase in mobility as ϕ_T increases to 0.5 is less intuitive, as semiflexible actin filaments are being replaced with more rigid microtubules. However, as described above, although the composite is becoming more rigid as ϕ_T increases, the effective mesh size ξ_C is increasing, allowing both actin and microtubules to more easily move. The competition between increasing rigidity and increasing ξ_C leads to a peak in mobility at $\phi_T = 0.5$.

It is important to note that the mobility trend is the same for actin and microtubules, indicating that the two filaments are sterically interacting and coupled to one another. For most composites, the microtubule mobility is less than that of actin, which is expected given the ~100-fold increase in its persistence length and bending rigidity (5,73). However, the difference in $\sigma_I/\langle I \rangle$ values for actin versus microtubules is less than a factor of two in all cases. Given the ~100-fold difference in bending compliance of the two filaments (5), which has been shown to be proportional to the rotational diffusion coefficient (73), this result is rather surprising and further demonstrates that the two filament networks are co-entangled and strongly coupled.

To determine if filament mobility is different on timescales above and below τ_e, we performed mobility analysis for movies with 0.033 s ($\sim 0.5\tau_e$) frames to compare to the 1 s ($\sim 14\tau_e$) frame movies used in Fig. 5 (Fig. S10). The mobility for both filaments is higher for $t < \tau_e$, which indicates that some of the fast relaxation modes, such as bending, become frozen out for $t > \tau_e$. Although microtubules cannot easily undergo bending fluctuations because of their extreme rigidity, they can undergo rotational diffusion on timescales below τ_e, which becomes restricted once the microtubules are subject to tube confinement (73). The rotational diffusion of actin filaments, which is faster than that of microtubules, could also be contributing to their mobility and explain their faster mobility compared to microtubules. Strictly speaking, $\tau_e \approx 0.07$ s is only valid for actin in $\phi_T = 0$ networks. However, computing the equivalent timescale for microtubules in $\phi_T = 1$ networks gives $\tau_{e,M} \approx 0.2$ s, which is still well below the 1 s frames used in our analysis. So, we expect to see a drop in the mobility of both actin and microtubules for 1 s frames versus 0.033 s frames as fast relaxation modes are being frozen out and filaments are only undergoing reptation. Finally, the fact that the nonmonotonic dependence on ϕ_T is preserved for times below τ_e is further evidence that increased concentrations of microtubules suppress actin bending modes, as at these short timescales, contributions from reptation are not yet present.

CONCLUSIONS

We use optical tweezers microrheology and two-color fluorescence microscopy to characterize the mesoscale force response and mobility of co-entangled composites of actin

and microtubules, which we create by in situ co-polymerization of actin monomers and tubulin dimers using custom-designed hybrid conditions. By systematically varying the relative concentrations of actin and microtubules (quantified by the molar fraction of tubulin ϕ_T), we show that composites exhibit a wide range of dynamical properties that can be tuned by ϕ_T. Our collective results demonstrate that microtubules suppress actin bending fluctuations, enabling composites to stiffen in response to strain and relax stress more slowly, whereas actin supports microtubules against buckling by providing a soft semiflexible mesh that permeates the larger microtubule mesh and partially absorbs stress. We also show that the interplay between varying mesh sizes and filament rigidity leads to emergent fast mobility in equimolar composites compared to networks of mostly actin or microtubules. Our quantitative analysis of the dependence of mechanical properties and mobility on composite composition provides important insights into how composite materials can be tuned to display user-defined mechanics.

Our results also demonstrate the synergistic ways in which thin, semiflexible actin filaments and thick, rigid microtubules can sterically interact to enable the myriad of mechanical processes and properties the cytoskeleton exhibits. In particular, structural interactions between actin and microtubules have been shown to be essential to cell migration, mitosis, apoptosis, and wound healing, as well as neuronal growth cone guidance and cortical flow in a wide range of cell types (1). Further, the role that Taxol plays in actin-microtubule mechanics during mitosis and apoptosis is of importance to the biomedical community, which uses Taxol to treat cancers (74,75). The concentrations of microtubules and actin, as well as the structural and mechanical properties of actin-microtubule composites, vary widely between cell types and in varying regions within each cell, yet their interactions appear highly conserved (1,76). Our in vitro platform offers an avenue for systematically probing these highly varied motifs, and our results provide the groundwork for future investigations on in vitro cytoskeletal composites that include cross-linking proteins, intermediate filaments, and motor proteins. These future studies will expand the phase space of mechanical properties that these bioinspired composite materials can exhibit and shed light onto the role that each additional component plays in the mechanics of the cytoskeleton.

SUPPORTING MATERIAL

Supporting Materials and Methods and 10 figures are available at http://www.biophysj.org/biophysj/supplemental/S0006-3495(18)30937-8.

AUTHOR CONTRIBUTIONS

S.N.R. designed experiments, conducted experiments, analyzed data, and wrote the manuscript. J.L.R. advised experimental design, analyzed and interpreted data, and helped write the manuscript. R.M.R.-A. designed, advised, and oversaw experiments; analyzed and interpreted data; and wrote the manuscript.

ACKNOWLEDGMENTS

This research was funded by a Scialog Collaborative Innovation Award from Research Corporation and the Gordon & Betty Moore Foundation (grant no. 24192, awarded to R.M.R.-A. and J.L.R.); a National Science Foundation CAREER Award (grant no. 1255446, awarded to R.M.R.-A.); and a National Institutes of Health R15 Award (National Institute of General Medical Sciences Award No. R15GM123420, awarded to R.M.R.-A.).

REFERENCES

1. Rodriguez, O. C., A. W. Schaefer, …, C. M. Waterman-Storer. 2003. Conserved microtubule-actin interactions in cell movement and morphogenesis. *Nat. Cell Biol.* 5:599–609.
2. Preciado López, M., F. Huber, …, M. Dogterom. 2014. Actin-microtubule coordination at growing microtubule ends. *Nat. Commun.* 5:4778.
3. Preciado López, M. P., F. Huber, …, G. H. Koenderink. 2014. In vitro reconstitution of dynamic microtubules interacting with actin filament networks. *Methods Enzymol.* 540:301–320.
4. Jensen, M. H., E. J. Morris, …, D. A. Weitz. 2014. Emergent properties of composite semiflexible biopolymer networks. *Bioarchitecture.* 4:138–143.
5. Gittes, F., B. Mickey, …, J. Howard. 1993. Flexural rigidity of microtubules and actin filaments measured from thermal fluctuations in shape. *J. Cell Biol.* 120:923–934.
6. Huber, F., A. Boire, …, G. H. Koenderink. 2015. Cytoskeletal crosstalk: when three different personalities team up. *Curr. Opin. Cell Biol.* 32:39–47.
7. McCullough, B. R., E. E. Grintsevich, …, E. M. De La Cruz. 2011. Cofilin-linked changes in actin filament flexibility promote severing. *Biophys. J.* 101:151–159.
8. De Gennes, P.-G. 1979. Scaling Concepts in Polymer Physics. Cornell University Press, Ithaca, NY.
9. Doi, M., and S. F. Edwards. 1988. The Theory of Polymer Dynamics. Oxford University Press, Oxford, UK.
10. Isambert, H., and A. Maggs. 1996. Dynamics and rheology of actin solutions. *Macromolecules.* 29:1036–1040.
11. Pelletier, V., N. Gal, …, M. L. Kilfoil. 2009. Microrheology of microtubule solutions and actin-microtubule composite networks. *Phys. Rev. Lett.* 102:188303.
12. Gardel, M. L., K. E. Kasza, …, D. A. Weitz. 2008. Chapter 19: mechanical response of cytoskeletal networks. *Methods Cell Biol.* 89:487–519.
13. Gurmessa, B., R. Fitzpatrick, …, R. M. Robertson-Anderson. 2016. Entanglement density tunes microscale nonlinear response of entangled actin. *Macromolecules.* 49:3948–3955.
14. Xu, J., Y. Tseng, and D. Wirtz. 2000. Strain hardening of actin filament networks. Regulation by the dynamic cross-linking protein α-actinin. *J. Biol. Chem.* 275:35886–35892.
15. Semmrich, C., R. J. Larsen, and A. R. Bausch. 2008. Nonlinear mechanics of entangled F-actin solutions. *Soft Matter.* 4:1675–1680.
16. Lin, Y.-C., G. H. Koenderink, …, D. A. Weitz. 2007. Viscoelastic properties of microtubule networks. *Macromolecules.* 40:7714–7720.
17. Gardel, M. L., M. T. Valentine, …, D. A. Weitz. 2003. Microrheology of entangled F-actin solutions. *Phys. Rev. Lett.* 91:158302.
18. Schmidt, C. F., M. Baermann, …, E. Sackmann. 1989. Chain dynamics, mesh size, and diffusive transport in networks of polymerized actin: a quasielastic light scattering and microfluorescence study. *Macromolecules.* 22:3638–3649.

19. Shabbir, S. H., M. M. Cleland, …, M. Mrksich. 2014. Geometric control of vimentin intermediate filaments. *Biomaterials.* 35:1359–1366.

20. Lin, Y.-C., G. H. Koenderink, …, D. A. Weitz. 2011. Control of nonlinear elasticity in F-actin networks with microtubules. *Soft Matter.* 7:902–906.

21. Wang, N., K. Naruse, …, D. E. Ingber. 2001. Mechanical behavior in living cells consistent with the tensegrity model. *Proc. Natl. Acad. Sci. USA.* 98:7765–7770.

22. Gupton, S. L., W. C. Salmon, and C. M. Waterman-Storer. 2002. Converging populations of f-actin promote breakage of associated microtubules to spatially regulate microtubule turnover in migrating cells. *Curr. Biol.* 12:1891–1899.

23. Dogterom, M., and B. Yurke. 1997. Measurement of the force-velocity relation for growing microtubules. *Science.* 278:856–860.

24. Gittes, F., E. Meyhöfer, …, J. Howard. 1996. Directional loading of the kinesin motor molecule as it buckles a microtubule. *Biophys. J.* 70:418–429.

25. Brangwynne, C. P., F. C. MacKintosh, …, D. A. Weitz. 2006. Microtubules can bear enhanced compressive loads in living cells because of lateral reinforcement. *J. Cell Biol.* 173:733–741.

26. Brangwynne, C. P., G. H. Koenderink, …, D. A. Weitz. 2008. Nonequilibrium microtubule fluctuations in a model cytoskeleton. *Phys. Rev. Lett.* 100:118104.

27. Das, M., and F. C. MacKintosh. 2011. Mechanics of soft composites of rods in elastic gels. *Phys. Rev. E Stat. Nonlin. Soft Matter Phys.* 84:061906.

28. Stricker, J., T. Falzone, and M. L. Gardel. 2010. Mechanics of the F-actin cytoskeleton. *J. Biomech.* 43:9–14.

29. Hawkins, T., M. Mirigian, …, J. L. Ross. 2010. Mechanics of microtubules. *J. Biomech.* 43:23–30.

30. Yang, Y., J. Lin, …, M. T. Valentine. 2012. Direct correlation between creep compliance and deformation in entangled and sparsely crosslinked microtubule networks. *Soft Matter.* 8:1776–1784.

31. Yang, Y., and M. T. Valentine. 2013. Determining the structure–mechanics relationships of dense microtubule networks with confocal microscopy and magnetic tweezers-based microrheology. *Methods Cell Biol.* 115:75–96.

32. Uhde, J., N. Ter-Oganessian, …, A. Boulbitch. 2005. Viscoelasticity of entangled actin networks studied by long-pulse magnetic bead microrheometry. *Phys. Rev. E Stat. Nonlin. Soft Matter Phys.* 72:061916.

33. Das, M., A. J. Levine, and F. MacKintosh. 2008. Buckling and force propagation along intracellular microtubules. *EPL.* 84:18003.

34. Gardel, M. L., J. H. Shin, …, D. A. Weitz. 2004. Elastic behavior of cross-linked and bundled actin networks. *Science.* 304:1301–1305.

35. Xu, J., D. Wirtz, and T. D. Pollard. 1998. Dynamic cross-linking by α-actinin determines the mechanical properties of actin filament networks. *J. Biol. Chem.* 273:9570–9576.

36. Falzone, T. T., and R. M. Robertson-Anderson. 2015. Active entanglement-tracking microrheology directly couples macromolecular deformations to nonlinear microscale force response of entangled actin. *ACS Macro Lett.* 4:1194–1199.

37. Valentine, M. T., Z. E. Perlman, …, D. A. Weitz. 2004. Colloid surface chemistry critically affects multiple particle tracking measurements of biomaterials. *Biophys. J.* 86:4004–4014.

38. Squires, T. M. 2008. Nonlinear microrheology: bulk stresses versus direct interactions. *Langmuir.* 24:1147–1159.

39. Weigand, W. J., A. Messmore, …, R. M. Robertson-Anderson. 2017. Active microrheology determines scale-dependent material properties of Chaetopterus mucus. *PLoS One.* 12:e0176732.

40. Chapman, C. D., K. Lee, …, R. M. Robertson-Anderson. 2014. Onset of non-continuum effects in microrheology of entangled polymer solutions. *Macromolecules.* 47:1181–1186.

41. Wyart, F. B., and P.-G. de Gennes. 2000. Viscosity at small scales in polymer melts. *Eur. Phys. J. E.* 1:93–97.

42. Cai, L. H., S. Panyukov, and M. Rubinstein. 2011. Mobility of nonsticky nanoparticles in polymer liquids. *Macromolecules.* 44:7853–7863.

43. Yamamoto, U., and K. S. Schweizer. 2011. Theory of nanoparticle diffusion in unentangled and entangled polymer melts. *J. Chem. Phys.* 135:224902.

44. Williams, M. C. 2002. Optical tweezers: measuring piconewton forces. Biophysics Textbook Online: https://www.biophysics.org/Portals/0/BPSAssets/Articles/williams.pdf.

45. Brau, R., J. Ferrer, …, M. Lang. 2007. Passive and active microrheology with optical tweezers. *J. Opt. A, Pure Appl. Opt.* 9:S103.

46. Segur, J. B., and H. E. Oberstar. 1951. Viscosity of glycerol and its aqueous solutions. *Ind. Eng. Chem.* 43:2117–2120.

47. Chapman, C. D., and R. M. Robertson-Anderson. 2014. Nonlinear microrheology reveals entanglement-driven molecular-level viscoelasticity of concentrated DNA. *Phys. Rev. Lett.* 113:098303.

48. Kikumoto, M., M. Kurachi, …, H. Tashiro. 2006. Flexural rigidity of individual microtubules measured by a buckling force with optical traps. *Biophys. J.* 90:1687–1696.

49. Lieleg, O., and A. R. Bausch. 2007. Cross-linker unbinding and self-similarity in bundled cytoskeletal networks. *Phys. Rev. Lett.* 99:158105.

50. Heidemann, K. M., A. Sharma, …, M. Wardetzky. 2015. Elasticity of 3D networks with rigid filaments and compliant crosslinks. *Soft Matter.* 11:343–354.

51. Schmoller, K. M., O. Lieleg, and A. R. Bausch. 2009. Structural and viscoelastic properties of actin/filamin networks: cross-linked versus bundled networks. *Biophys. J.* 97:83–89.

52. Bai, M., A. R. Missel, …, A. J. Levine. 2011. The mechanics and affine–nonaffine transition in polydisperse semiflexible networks. *Soft Matter.* 7:907–914.

53. Hu, Y., X. Zhao, …, Z. Suo. 2010. Using indentation to characterize the poroelasticity of gels. *Appl. Phys. Lett.* 96:121904.

54. Kalcioglu, Z. I., R. Mahmoodian, …, K. J. Van Vliet. 2012. From macro-to microscale poroelastic characterization of polymeric hydrogels via indentation. *Soft Matter.* 8:3393–3398.

55. Moeendarbary, E., L. Valon, …, G. T. Charras. 2013. The cytoplasm of living cells behaves as a poroelastic material. *Nat. Mater.* 12:253–261.

56. Gittes, F., B. Schnurr, …, C. F. Schmidt. 1997. Microscopic viscoelasticity: shear moduli of soft materials determined from thermal fluctuations. *Phys. Rev. Lett.* 79:3286–3289.

57. Schmidt, F. G., B. Hinner, and E. Sackmann. 2000. Microrheometry underestimates the values of the viscoelastic moduli in measurements on F-actin solutions compared to macrorheometry. *Phys. Rev. E Stat. Phys. Plasmas Fluids Relat. Interdiscip. Topics.* 61:5646–5653.

58. Das, M., and F. C. Mackintosh. 2010. Poisson's ratio in composite elastic media with rigid rods. *Phys. Rev. Lett.* 105:138102.

59. Robison, P., M. A. Caporizzo, …, B. L. Prosser. 2016. Detyrosinated microtubules buckle and bear load in contracting cardiomyocytes. *Science.* 352:aaf0659.

60. Yang, Y., M. Bai, …, M. T. Valentine. 2013. Microrheology of highly crosslinked microtubule networks is dominated by force-induced crosslinker unbinding. *Soft Matter.* 9:383–393.

61. Needleman, D. J., M. A. Ojeda-Lopez, …, C. R. Safinya. 2004. Higher-order assembly of microtubules by counterions: from hexagonal bundles to living necklaces. *Proc. Natl. Acad. Sci. USA.* 101:16099–16103.

62. Tang, J. X., and P. A. Janmey. 1996. The polyelectrolyte nature of F-actin and the mechanism of actin bundle formation. *J. Biol. Chem.* 271:8556–8563.

63. Tang, J. X., S. Wong, …, P. A. Janmey. 1996. Counterion induced bundle formation of rodlike polyelectrolytes. *Ber. Bunsenges. Phys. Chem.* 100:796–806.

64. Hoffman, B. D., and J. C. Crocker. 2009. Cell mechanics: dissecting the physical responses of cells to force. *Annu. Rev. Biomed. Eng.* 11:259–288.

65. Robertson, R. M., and D. E. Smith. 2007. Direct measurement of the intermolecular forces confining a single molecule in an entangled polymer solution. *Phys. Rev. Lett.* 99:126001.

66. Broedersz, C. P., M. Depken, …, F. C. MacKintosh. 2010. Cross-link-governed dynamics of biopolymer networks. *Phys. Rev. Lett.* 105:238101.

67. Sussman, D. M., and K. S. Schweizer. 2013. Entangled rigid macromolecules under continuous startup shear deformation: consequences of a microscopically anharmonic confining tube. *Macromolecules.* 46:5684–5693.

68. Käs, J., H. Strey, and E. Sackmann. 1994. Direct imaging of reptation for semiflexible actin filaments. *Nature.* 368:226–229.

69. Wang, B., J. Guan, …, S. Granick. 2010. Confining potential when a biopolymer filament reptates. *Phys. Rev. Lett.* 104:118301.

70. Odijk, T. 1986. Theory of lyotropic polymer liquid crystals. *Macromolecules.* 19:2313–2329.

71. Falzone, T. T., S. Blair, and R. M. Robertson-Anderson. 2015. Entangled F-actin displays a unique crossover to microscale nonlinearity dominated by entanglement segment dynamics. *Soft Matter.* 11:4418–4423.

72. Sussman, D. M., and K. S. Schweizer. 2012. Microscopic theory of quiescent and deformed topologically entangled rod solutions: general formulation and relaxation after nonlinear step strain. *Macromolecules.* 45:3270–3284.

73. Fakhri, N., F. C. MacKintosh, …, M. Pasquali. 2010. Brownian motion of stiff filaments in a crowded environment. *Science.* 330:1804–1807.

74. Jordan, M. A., and L. Wilson. 2004. Microtubules as a target for anticancer drugs. *Nat. Rev. Cancer.* 4:253–265.

75. Jordan, M. A., R. J. Toso, …, L. Wilson. 1993. Mechanism of mitotic block and inhibition of cell proliferation by taxol at low concentrations. *Proc. Natl. Acad. Sci. USA.* 90:9552–9556.

76. Blanchoin, L., R. Boujemaa-Paterski, …, J. Plastino. 2014. Actin dynamics, architecture, and mechanics in cell motility. *Physiol. Rev.* 94:235–263.

Biophysical Journal, Volume *115*

Supplemental Information

Co-Entangled Actin-Microtubule Composites Exhibit Tunable Stiffness and Power-Law Stress Relaxation

Shea N. Ricketts, Jennifer L. Ross, and Rae M. Robertson-Anderson

Supplemental Information

Co-entangled actin-microtubule composites exhibit tunable nonlinear stiffness and power-law stress relaxation

Shea N. Ricketts[a], Jennifer L. Ross[b] and Rae M. Robertson-Anderson[*a]

Optimization of Composite Conditions: We sought to create conditions in which (1) both tubulin dimers and actin monomers could polymerize into filaments of lengths ~2 – 30 μm, and (2) both filaments could co-entangle with each other to create isotropic, well-mixed networks with no appreciable phase separation or bundling.

Buffer Conditions: We first tested standard actin network buffer "F-buffer" (10 mM Imidazole (pH 7.0), 50 mM KCl, 1 mM $MgCl_2$, 1 mM EGTA, 0.2 mM ATP) and standard microtubule buffer "PEM" (100 mM PIPES (pH 6.8), 2 mM $MgSO_4$, 2 mM EGTA, 1 mM GTP, 5 μM Taxol). With each of these standard buffers, the other filament did not polymerize. We also tried F-buffer with varying concentrations of GTP to promote microtubule polymerization. However, in all tested cases, the tubulin formed large denatured aggregates. We also tried PEM with varying concentrations of ATP added. For standard ATP concentrations used in F-buffer (0.4 mM), no actin filaments formed, but when ATP concentration was increased to 2 mM and $MgSO_4$ was replaced with $MgCl_2$, actin monomers polymerized into filaments that appeared entangled with the microtubules (Figs S1 and S2).

Polymerization Conditions: Actin polymerization is typically carried out for 1 hour at room temperature (20°C) whereas microtubule polymerization requires incubation at 37°C for 30 minutes. We tested temperatures between 20 °C and 37 °C and times from 30 to 90 mins. We found that 37°C was indeed needed for tubulin to polymerize (and did not inhibit actin polymerization), but an incubation time of 60 minutes rather than 30 minutes led to longer actin filaments without affecting the microtubule length. Longer incubation times did not result in appreciably longer filaments.

Validation: As shown in Figure S3, we measured the lengths of actin and microtubules in the composites. We found that the measured actin lengths were similar to those measured in F-buffer with similar actin concentrations and polymerization conditions (see Refs 12 and 70 in manuscript). Measured microtubule lengths are also comparable to those measured in canonical microtubule buffer conditions at similar tubulin concentrations (see Ref 28). We also carried out force measurements for actin networks ($\phi_T = 0$) in F-buffer and microtubule networks ($\phi_T = 1$) in PEM, both with their standard polymerization conditions. As shown in Figure S4 we see comparable measured force responses for our conditions and the canonical conditions. We have also imaged networks in canonical conditions and see little difference from our conditions (Fig S4).

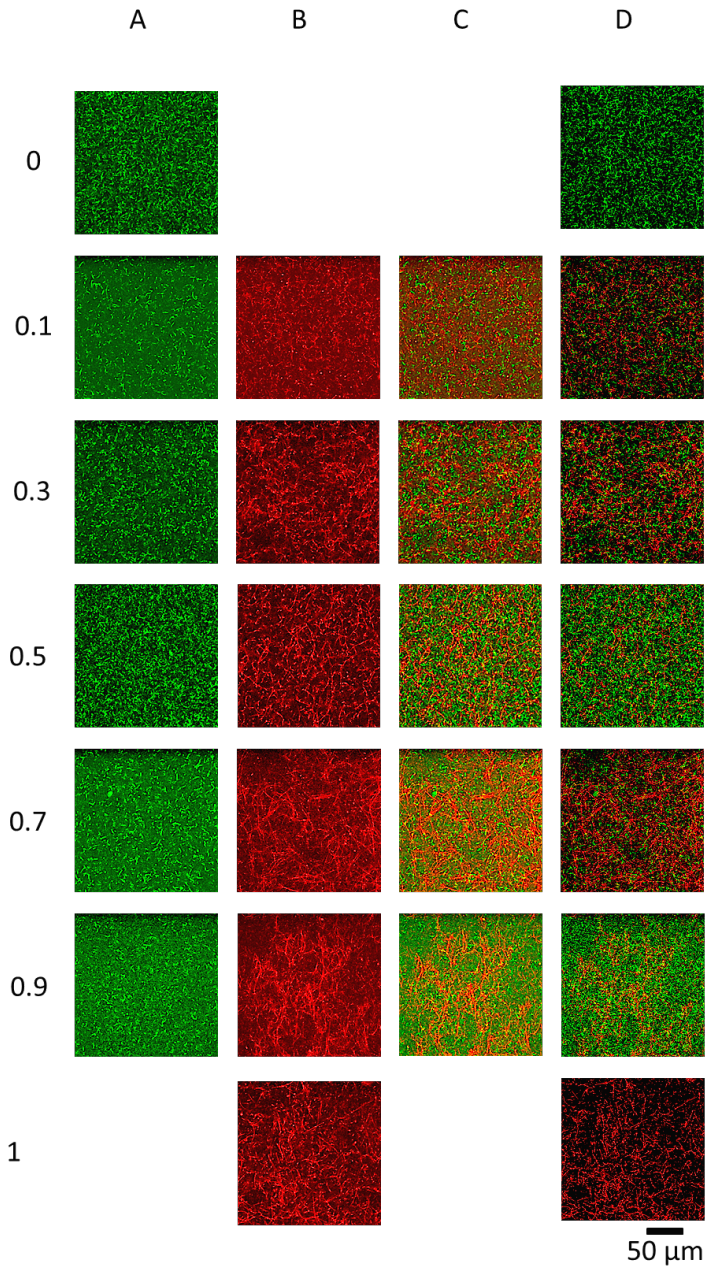

FIGURE S1. Two-color laser scanning confocal imaging of co-entangled composites of actin and microtubules. 512x512 images of actin-microtubule composites taken on a Nikon A1R laser scanning confocal microscope with 60*x* objective and QImaging CCD camera. Total protein concentration is 11.6 µM in all images, with 0.13 µM of actin and microtubules labeled with Alexa-488 (green) and rhodamine (red), respectively. Scale bars are 50 µm and apply to all images. Each row corresponds to a composite with a different tubulin fraction, ϕ_T, listed to the left of each row. From left to right of each row shows: (A) the actin (green) channel, (B) the microtubule (red) channel, (C) both channels, and (D) the binary skeletonization of two-color images shown in C. As shown actin and microtubules both form percolating networks that co-localize with each other. All composites appear homogeneous with no apparent phase separation or clustering.

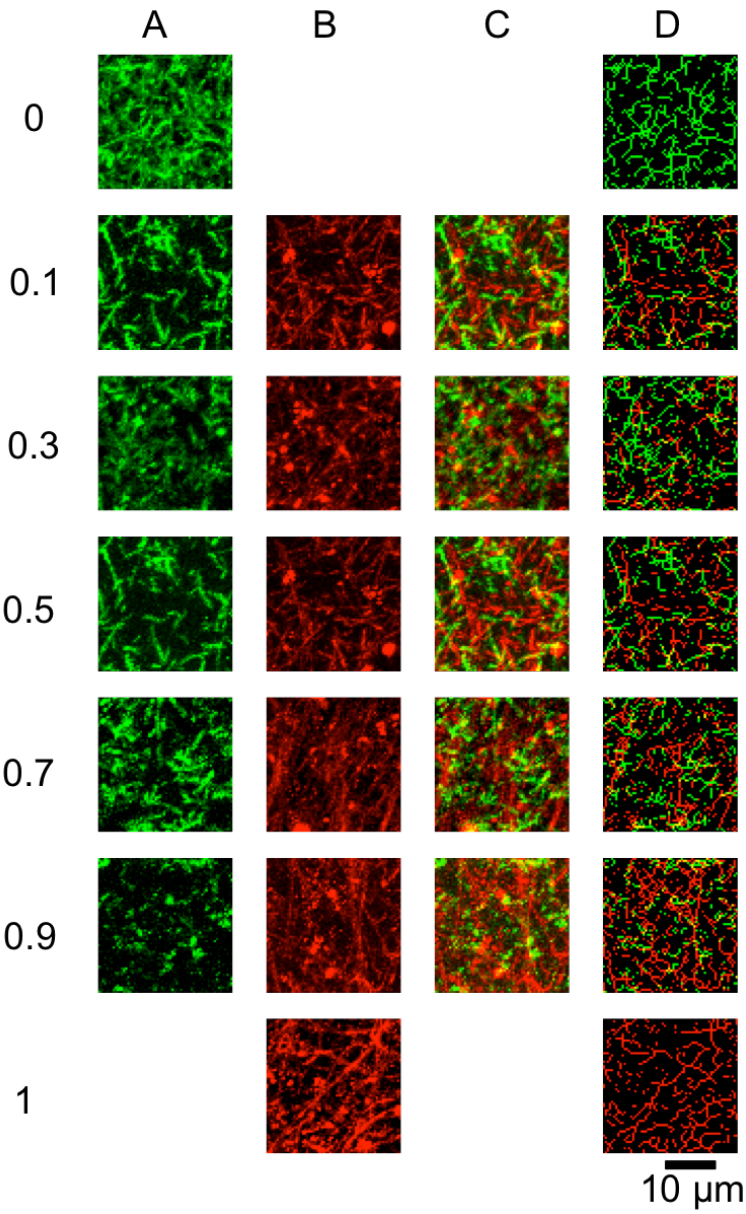

FIGURE S2. Three-dimensional structure of co-entangled actin-microtubule composites. Maximum intensity projection images from 64-voxel z-stacks of actin-microtubule composites to show 3D structure of composites. Image acquisition, processing and analysis are described in Methods and Fig S1 caption. Scale bar is 10 μm and applies to all images. Each row corresponds to a composite with a different tubulin fraction, ϕ_T, listed to the left of each row. From left to right of each row shows: the maximum intensity projections of the (A) actin (green) channel, (B) microtubule (red) channel, and (C) both channels, as well as (D) the binary skeletonization of two-color maximum projection images shown in C. Images show the 3D network connectivity and architecture. As shown actin and microtubules both form percolating networks that co-localize with each other. All composites appear homogeneous with no apparent phase separation or clustering.

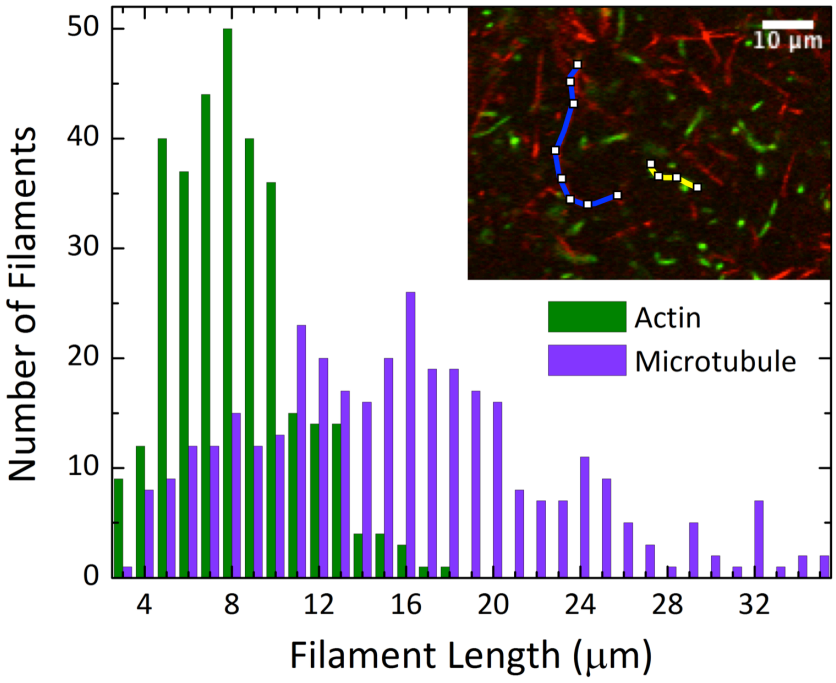

FIGURE S3. Measured actin and microtubule contour lengths within composites. Images were taken on the surface of the sample chamber and only filaments that were adhered to the surface (visibly immobile) were measured (as shown in inset). Fluorescent labeling and image acquisition methods are the same as those used in Fig S1. A total of 350 microtubules and actin filaments in each composite were measured using Fiji (as depicted in the inset). Measured lengths of microtubules and actin are 18.8 +/- 9.7 μm and 8.7 +/- 2.8 μm, respectively. The distribution shown is for a $\phi_T = 0.5$ composite, but similar length distributions were measured for all composites.

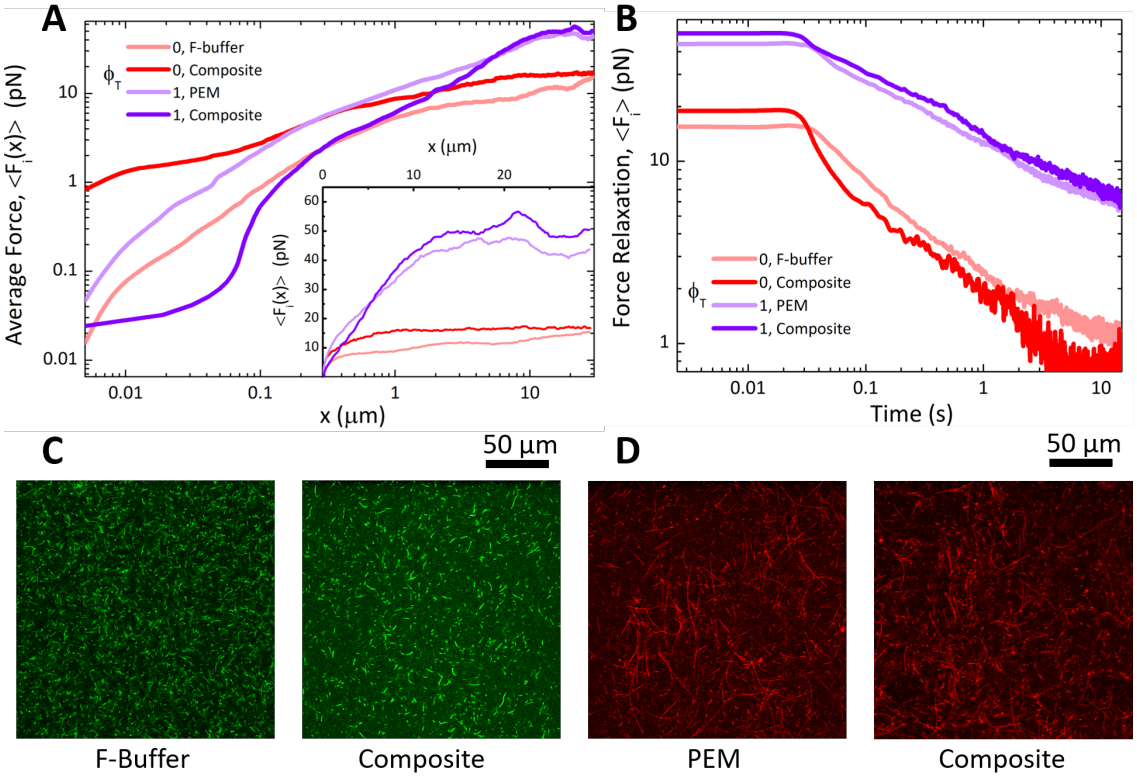

FIGURE S4. Force measurements and images of actin and microtubules in composite buffer and canonical buffer conditions. (A) Force applied to the moving bead by: actin networks (ϕ_T = 0) in F-buffer and composite buffer, and microtubule networks (ϕ_T = 1) in PEM and composite buffer. (B) Corresponding force relaxation for systems shown in A. All curves shown in A and B are averages of 25 individual trials. (C,D) Confocal images of actin networks (ϕ_T = 0) in F-buffer and composite buffer (C) and microtubule networks (ϕ_T = 1) in PEM and composite buffer (D). Scale bar is 50 μm and applies to all images.

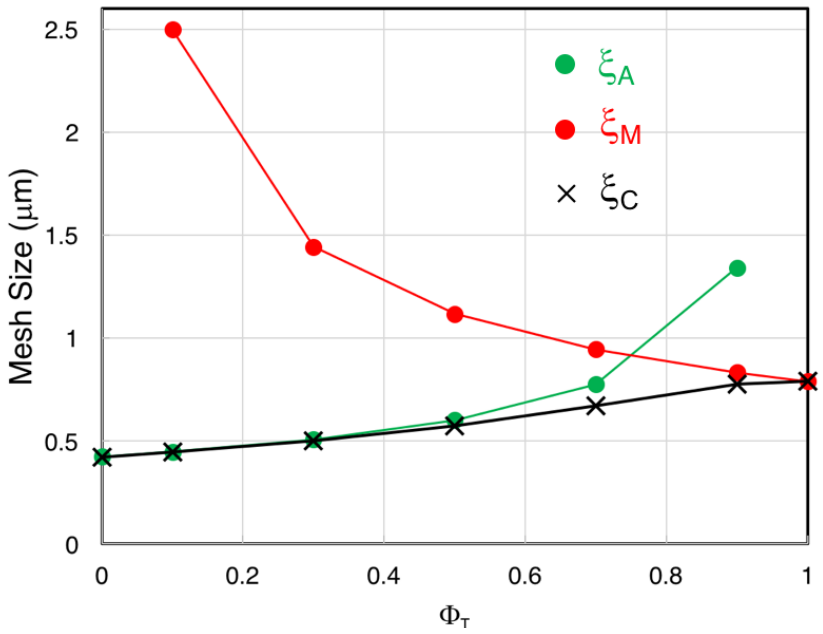

FIGURE S5: Predicted mesh sizes for actin and microtubules, as well as the effective composite mesh size, for composites of varying ϕ_T. The predicted mesh size for actin (green circles) is calculated as $\xi_A = 0.3/c_A^{1/2}$ and predicted mesh size for microtubules (red circles) is calculated as $\xi_M = 0.89/c_T^{1/2}$. The effective composite mesh (black crosses) is calculated as $\xi_C = (\xi_M^{-3}+\xi_A^{-3})^{-1/3}$. As shown ξ_C increases with increasing ϕ_T. The actin mesh size remains smaller than ξ_M and comparable to ξ_C for all composites until the fraction of microtubules exceeds 70% of the total molar mass ($\phi_T > 0.7$).

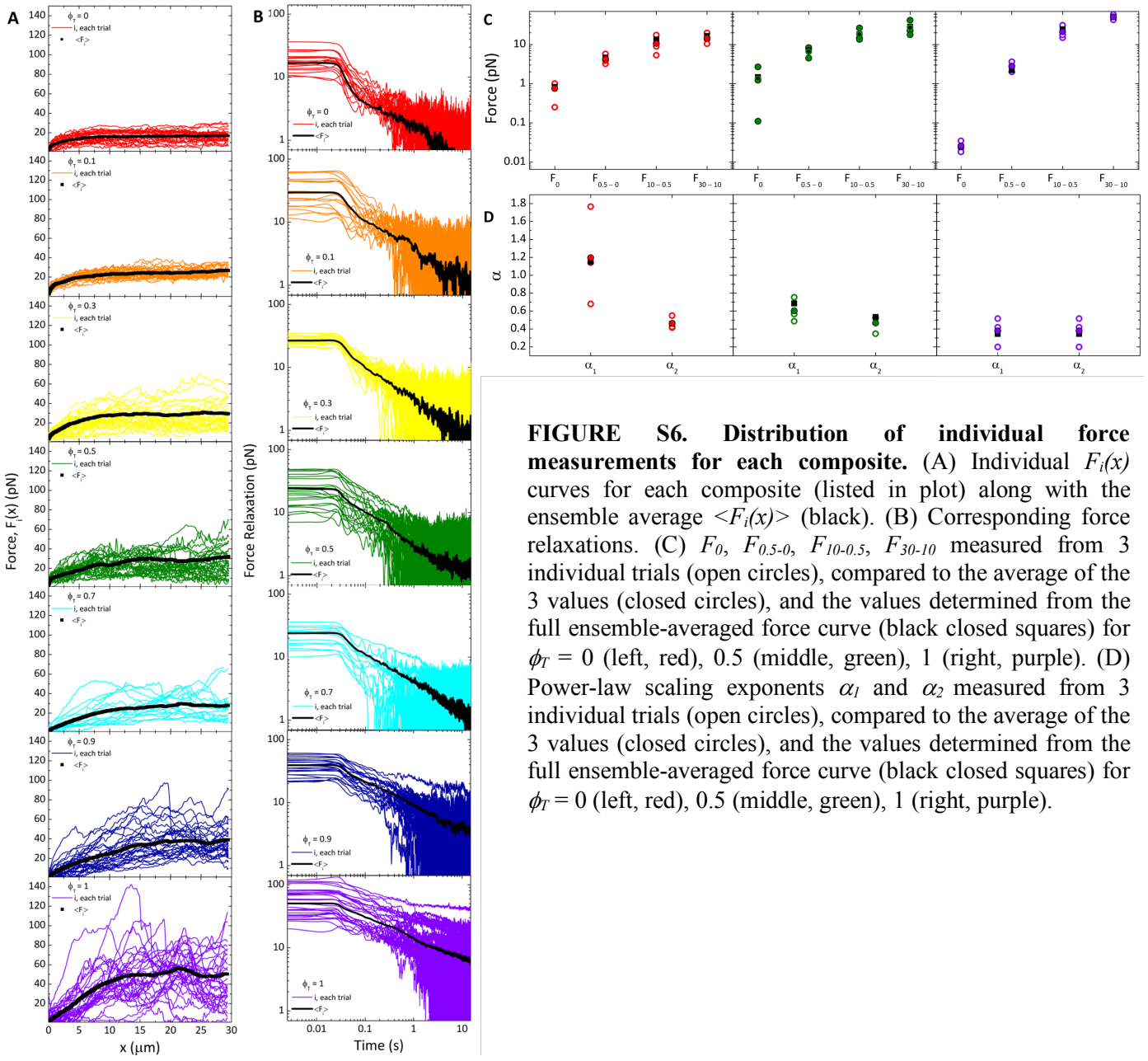

FIGURE S6. Distribution of individual force measurements for each composite. (A) Individual $F_i(x)$ curves for each composite (listed in plot) along with the ensemble average $\langle F_i(x) \rangle$ (black). (B) Corresponding force relaxations. (C) F_0, $F_{0.5\text{-}0}$, $F_{10\text{-}0.5}$, $F_{30\text{-}10}$ measured from 3 individual trials (open circles), compared to the average of the 3 values (closed circles), and the values determined from the full ensemble-averaged force curve (black closed squares) for ϕ_T = 0 (left, red), 0.5 (middle, green), 1 (right, purple). (D) Power-law scaling exponents α_1 and α_2 measured from 3 individual trials (open circles), compared to the average of the 3 values (closed circles), and the values determined from the full ensemble-averaged force curve (black closed squares) for ϕ_T = 0 (left, red), 0.5 (middle, green), 1 (right, purple).

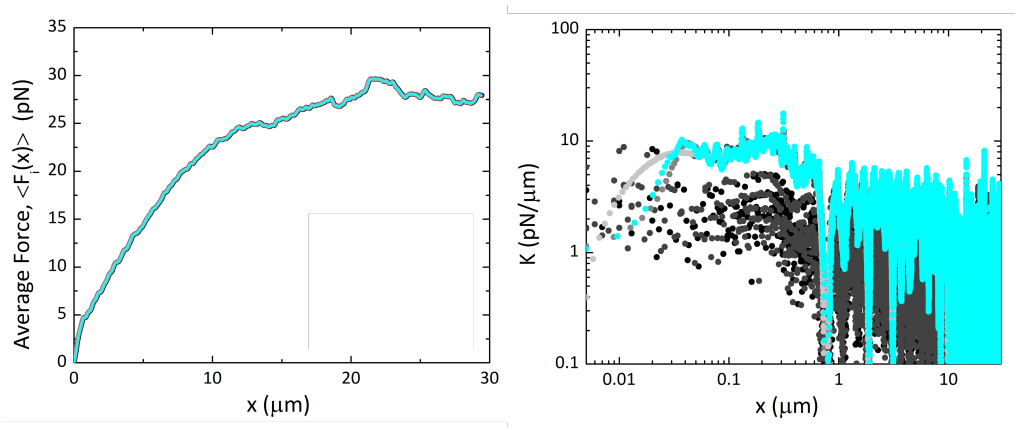

FIGURE S7. The effect of Gaussian smoothing on the measured force data. Measured force (left) and differential modulus (right) for ϕ_T = 0.7 composites with different degrees of Gaussian smoothing: no smoothing (black), 10 data point sliding window (dark grey), 20 data point sliding window (cyan), 25 point sliding window (grey), 100 data point sliding window executed 3 times (light grey).

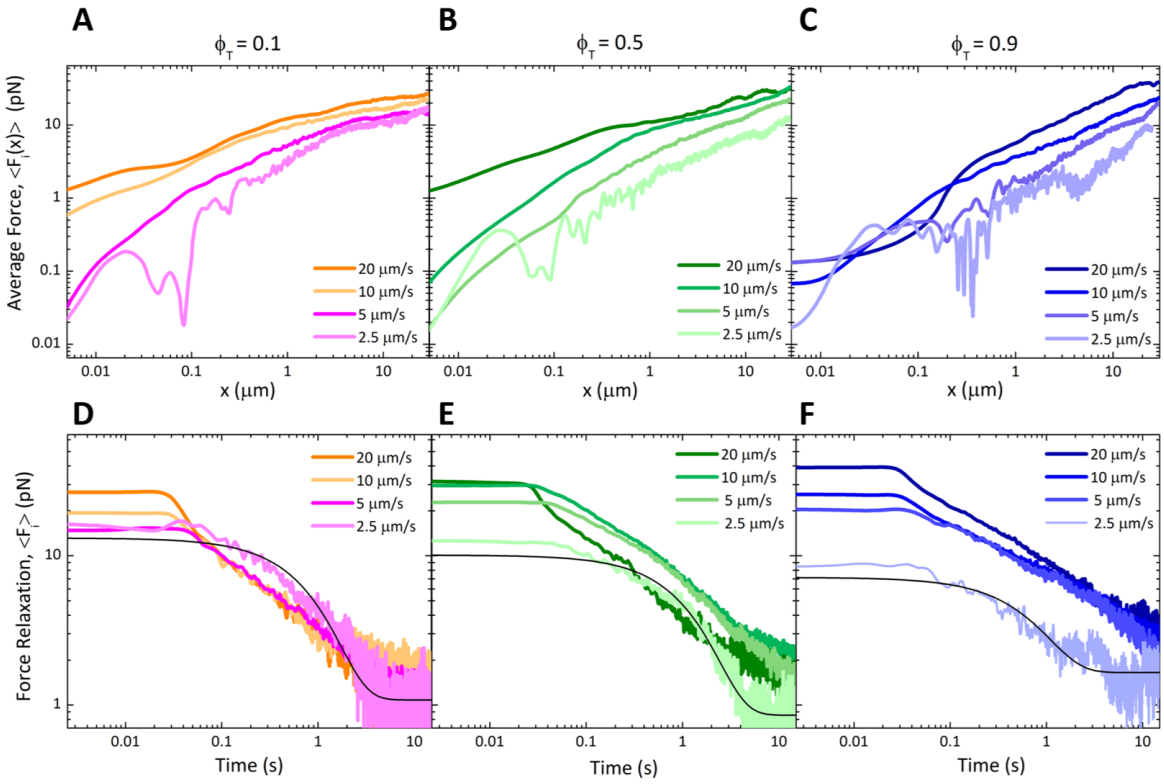

FIGURE S8. Dependence of force response and relaxation on the speed of the bead displacement. The resistive force during bead displacement (A-C) and subsequent force relaxation (D-F) for bead displacement speeds of 2.5, 5, 10 and 20 μm/s. Data for ϕ_T = 0.1 (A,D), 0.5 (B,E) and 0.9 (C,F) are shown. The noise displayed in A-C for the 2.5 μm/s curves is due to the small signal measured at this slow speed. As shown in (D-F) relaxation curves transition from power-law to exponential (black lines) at a speed of 2.5 – 5 μm/s.

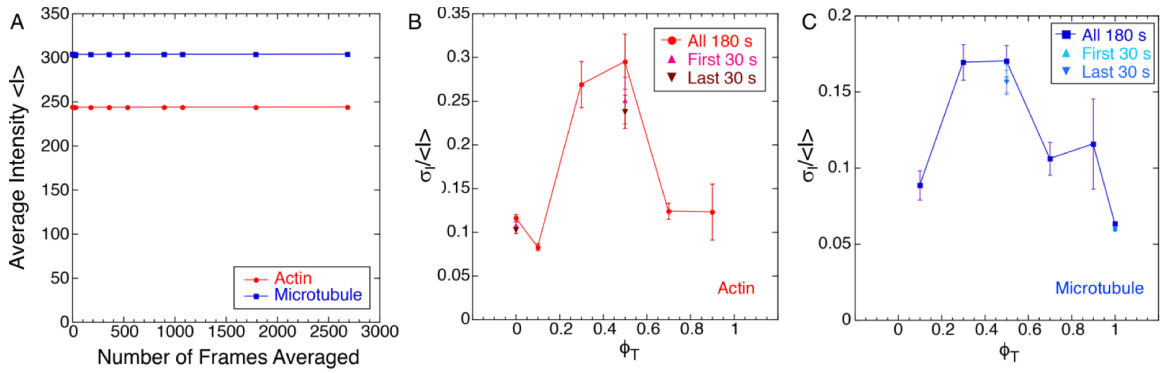

FIGURE S9. The effect of photobleaching on imaging and mobility analysis. To determine if photobleaching has an impact on the image analysis presented in Figure 5, we evaluate (A) the average pixel intensity of images over different time intervals and (B, C) the variation between mobility analysis performed on the beginning versus the end of movies. All imaging and analysis details are provided in Methods. (A) The average pixel intensity $<I>$ for the actin (red) and microtubule (blue) channels of 5400-frame movies averaged over varying numbers of frames. As shown the average intensity is essentially unchanged for much of the time course of movies, demonstrating that photobleaching is minimal. (B) Mobility, $\sigma_I/<I>$, versus ϕ_T for the actin channel, computed for the first 30 s (upright triangles), last 30 s (inverted triangles), and entire 180 s (circles) of movies. (C) The same data as in B for the microtubule channel. As shown, the data for the first 30 s, last 30 s, and entire movie fall within the error bars of each other in all cases measured demonstrating that any photobleaching or time-dependent variations in intensity do not affect our measurements. Further, typical average intensity values for our movies are ~200 – 300 counts and standard deviations are ~20 – 60 counts so our measurements are well above the 5.5 count noise floor of our camera.

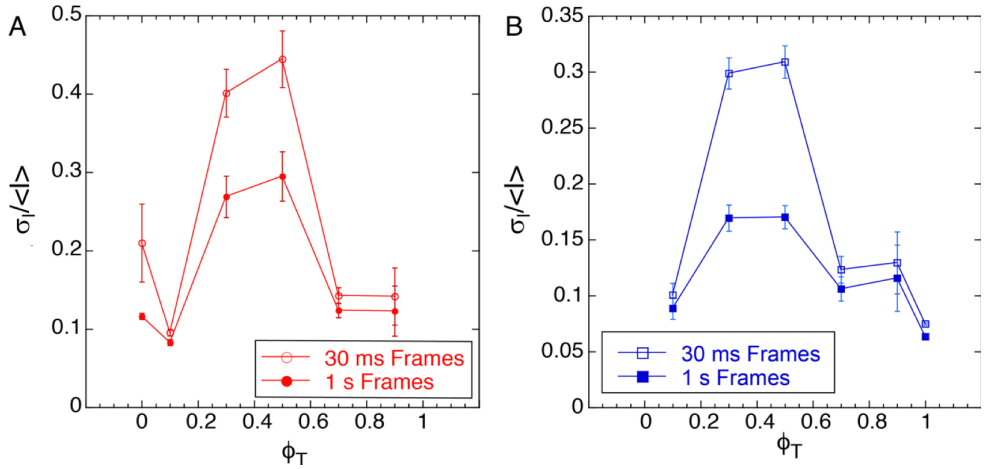

Figure S10: Mobility calculations for varying time windows above and below the entanglement time τ_e. Mobility, $\sigma_I/<I>$, versus ϕ_T for the (A) actin channel and (B) microtubule channel using a time resolution of 0.033 s (1 frame) compared to 1 s (30 frames averaged together). Imaging and analysis details are provided in Methods. As shown, the non-monotonic dependence of mobility of both actin and microtubules on ϕ_T is robust to varying time windows used for analysis. However, for times below τ_e the mobility of both actin and microtubules is enhanced. Decreased mobility for times longer than τ_e is expected as faster relaxation modes, such as bending, are predicted to be frozen out at these timescales.